Testing general relativity with LISA including spin precession and higher harmonics in the waveform

Huwyler, Cédric ; Klein, Antoine ; Jetzer, Philippe

Abstract: We compute the accuracy at which a Laser Interferometer Space Antenna-like space-based gravitational wave detector will be able to observe deviations from general relativity in the low frequency approximation. To do so, we introduce six correction parameters that account for modified gravity in the second post-Newtonian gravitational wave phase for inspiralling supermassive black hole binaries with spin precession on quasicircular orbits. Our implementation can be regarded as a subset of the parametrized post-Einsteinian formalism developed by Yunes and Pretorius, being able to investigate also next-to-leading order effects. In order to find error distributions for the alternative theory parameters, we use the Fisher information formalism and carry out Monte Carlo simulations for 17 different binary black hole mass configurations in the range 105Msun<M<108Msun with 103 randomly distributed points in the parameter space each, comparing the full (FWF) and restricted (RWF) versions of the gravitational waveform. We find that the binaries can roughly be separated into two groups: one with low (107Msun) and one with high total masses (107Msun). The RWF errors on the alternative theory parameters are 2 orders of magnitude higher than the FWF errors for high-mass binaries while almost comparable for low-mass binaries. Because of dilution of the available information, the accuracy of the binary parameters is reduced by factors of a few, except for the luminosity distance, which is affected more seriously in the high-mass regime. As an application as well as to compare our research with previous work, we compute an optimal lower bound on the graviton Compton wavelength, which is increased by a factor of ˜1.6 when using the FWF.

DOI: https://doi.org/10.1103/PhysRevD.86.084028

Testing General Relativity with LISA including Spin Precession and Higher Harmonics in the Waveform

Cédric Huwyler,* Antoine Klein, and Philippe Jetzer
Institut für Theoretische Physik, Universität Zürich, Winterthurerstrasse 190, 8057 Zürich
(Dated: August 23, 2012)

We compute the accuracy at which a LISA-like space-based gravitational wave detector will be able to observe deviations from General Relativity in the low frequency approximation. To do so, we introduce six correction parameters that account for modified gravity in the second post-Newtonian gravitational wave phase for inspiralling supermassive black hole binaries with spin precession on quasi-circular orbits. Our implementation can be regarded as a subset of the ppE formalism developed by Yunes and Pretorius, being able to investigate also next-to-leading order effects. In order to find error distributions for the alternative theory parameters, we use the Fisher information formalism and carry out Monte Carlo simulations for 17 different binary black hole mass configurations in the range $10^5 M_\odot < M < 10^8 M_\odot$ with 10^3 randomly distributed points in the parameter space each, comparing the full (FWF) and restricted (RWF) version of the gravitational waveform. We find that the binaries can roughly be separated into two groups: one with low ($\lesssim 10^7 M_\odot$) and one with high total masses ($\gtrsim 10^7 M_\odot$). The RWF errors on the alternative theory parameters are two orders of magnitude higher than the FWF errors for high-mass binaries while almost comparable for low-mass binaries. Due to dilution of the available information, the accuracy of the binary parameters is reduced by factors of a few, except for the luminosity distance which is affected more seriously in the high-mass regime. As an application and to compare our research with previous work, we compute an optimal lower bound on the graviton Compton wavelength which is increased by a factor of ~ 1.6 when using the FWF.

PACS numbers: 04.30.Db, 04.50.Kd

I. INTRODUCTION

Although General Relativity (GR) has so far passed all experimental and observational tests [1], some unsatisfactorily explained phenomena still remain which could be more elegantly described by alternative gravity theories. Among these theories are the proposed inflationary epoch of the universe shortly after the big bang which explains the temperature homogeneity of the cosmic microwave background, dark matter which should account for the missing 23% of the mass in the universe and dark energy introduced as an attempt to drive the observed late accelerated expansion of the universe. Moreover, attempts to quantize GR or to unify gravitation with the other three fundamental forces are as yet incomplete. Consequently, several modifications to GR have been proposed. Certain alternative theories work by introducing additional fields to the Einstein-Hilbert action of GR. Scalar-tensor field theories such as Brans-Dicke theory [2] are candidates for reproducing inflation. Modified Newtonian Dynamics (MOND) [3] attempts to get rid of dark matter by modifying the $1/r^2$ behavior of the gravitational potential; a relativistic version introducing scalar and vector fields called Tensor-Vector-Scalar gravity (TeVeS) has also been proposed [4]. The class of $f(R)$ theories [5] modify the Einstein-Hilbert action by replacing the Riemann scalar by a function of it. More phenomenological approaches such as Massive Graviton theories [6, 7] study the wave propagation of a 'massive' gravitational field.

Since alternatives to GR can be heavily constrained by the observation of Solar System effects and pulsar binaries [1], viable alternative theory candidates should reduce to GR in the limit of weak fields. In spacetime regions with strong dynamical gravity, such as binary black holes (BBHs), comparable constraints do not yet exist and should be tested for. A good review of currently discussed alternatives to GR can be found in the appendix of [8].

Among the most popular gravitational wave detectors are laser interferometers. Several ground-based interferometers such as LIGO (USA), Virgo (Italy) and GEO600 (Germany) have been built and are already operating, being sensitive to high frequencies between 10 Hz and 1 kHz. Currently LIGO is being upgraded to *Advanced LIGO* with a sensitivity ten times better, and is expected to observe several events per year and make gravitational wave detection likely within the next five years. Hence gravitational waves could finally be observed directly a hundred years after their theoretical prediction by Einstein.

Complementary to ground-based detectors restricted by their short arm-length and seismic noise at low frequencies, the spaceborne, low frequency detector eLISA/NGO (evolved Laser Interferometer Space Antenna / Next Gravitational Wave Observatory) has been proposed, sensitive in a range of $\sim 10^{-5} - 1$ Hz. The mission was originally planned as an ESA/NASA collaboration, consisting of three spacecrafts separated by five million km, forming an equilateral triangle of laser arms.

*Electronic address: chuwyler@physik.uzh.ch

In 2011, NASA discontinued their participation in the LISA project; the European Space Agency planned to realize the project on their own with a reduced, affordable mission design called eLISA/NGO [9]. Although not selected as the first large L1 mission, there is a high chance that eLISA/NGO will be selected within the next few years as an L2 mission. In this paper we perform calculations for the originally planned LISA-like detector, as this enables us to compare our results to other studies and also since it is currently unknown with what technical specifications eLISA will fly. We will use the term 'LISA' for a classic LISA-like mission throughout this paper.

Among the strongest sources which LISA will detect are supermassive black hole binaries with masses between $10^5 - 10^7 M_\odot$. After a long inspiral phase, such binaries could merge into one single Kerr black hole which rings down from its excited state by emitting gravitational radiation. Compact binary inspirals produce a very clean and long-lasting gravitational signal which may be accurately described by harmonics of the orbital phase using the post-Newtonian (PN) formalism. Inspiralling BBHs emit gravitational radiation carrying information about binary parameters such as the individual black hole masses and spins in its amplitude and phase. By using matched filtering techniques [10, 11], the binary parameters can be extracted from the noisy signal measured by the detector. Alternative gravity theories will also leave their imprints on gravitational waves, since they modify the strong-field dynamics of the BBH, resulting in a different orbital phase evolution. Also a possible 'graviton mass' will influence gravitational waves on their way to us by making their velocity frequency dependent. Since alternative theories are heavily constrained and LISA is expected to observe signals with very high signal-to-noise ratio (SNR), a signal from a BBH will be detected with GR waveform templates regardless whether or not GR is true. This could create a fundamental bias [8] in parameter extraction if the signal is fitted with an incorrect GR waveform template, leading to incorrect parameter estimation. To fix this bias, additional parameters controlling deviations from GR can be introduced. Adding parameters while having the same information from the detectors increases the correlation between the extracted parameters and thus decreases the accuracy in the recovered parameter values.

Previous papers computed bounds which LISA could place on the Brans-Dicke parameter $\omega_{\rm BD}$ (see e.g. [12, 13]) or on the graviton Compton wavelength λ_g (see e.g. [6]) using matched filtering. Due to the no hair theorem, for BBHs, scalar field effects in Brans-Dicke theory arising from the inner structure of compact objects cannot be distinguished; however, such massive binaries are an excellent environment to test massive gravity effects. The effects of 'massive' propagation have been investigated by various authors, considering different source and detector models. After a first analysis of massive graviton propagation by Will [6], Berti et al. [14] introduced spin parameters and spin-orbit/spin-spin couplings, finding a loss of accuracy due to the extra parameters included in the model. Stavridis and Will [7] considered the full precession of the spins and discovered that the resulting phase modulation restores the lost accuracy on λ_g. Yagi and Tanaka [15] included eccentricity to the system and found that the additional structure through both precession and eccentricity increases the measurement accuracy by an order of magnitude. Arun and Will [16] showed that the bounds on λ_g are improved by almost an order of magnitude for non-spinning BBHs when using the full waveform (FWF) instead of the restricted waveform (RWF) which takes the phase up to full PN order but considers the amplitude only to leading order. Taking higher harmonics into consideration increases the time during which the signal stays in the frequency window of LISA and shows a richer structure in the gravitational wave, leading to less correlation in the parameter space. Keppel and Ajith [17] used hybrid inspiral-merger-ringdown waveforms and found that they lead to a ~ 10 times higher accuracy than for inspiral-only waveforms. Moreover, Berti et al. [18] pointed out that the combination of the bounds on λ_g from individually observed inspirals in a two-year running time can again raise the accuracy by an order of magnitude. Tables summarizing lower bounds on λ_g and upper bounds on $\omega_{\rm BD}$ found by previous works are e.g. provided by [15, 17]. Arun et al. [19] re-interpreted the matched filtering method and fitted the post-Newtonian coefficients to the waveform instead of the parameters usually extracted from them. They discussed to what extent LISA will be able to measure deviations from the 3.5PN gravitational wave phase parameters in General Relativity. Yunes and Pretorius [8] generalized this approach to a *parameterized post-Einsteinian (ppE)* formalism which maps different types of alternative theories to the gravitational waveform of a compact binary merger. Cornish et al. [20] used Markov Chain Monte Carlo simulations to investigate parameter biases and possible bounds on the ppE parameters.

In this work we parametrize alternative theories by introducing corrections to the post-Newtonian coefficients of the orbital phase for a BBH inspiral, including the full 2PN precession of spins and angular momentum. We add higher harmonics to the waveform by considering the full 2PN amplitude. We postpone the discussion of eccentric orbits to later work and restrict our calculations to quasi-circular orbits. Since matched filtering is far more sensitive to the gravitational wave phase than to the amplitude, we do not consider corrections to the amplitude of the wave. We evaluate the measurement accuracy with which a LISA-like mission will be able to detect such corrections for BBHs. To estimate the errors on the parameters, we make use of the Fisher information formalism which is legitimate in the limit of high SNR which LISA will provide.

The organization of this paper is as follows. In Sec. II we shortly introduce the necessary equations to de-

scribe the evolution of the inspiral phase, the spins and the angular momentum of a BBH up to 2PN. In Sec. III we introduce small departures from GR into the post-Newtonian frequency evolution equation. We then compute the modified orbital phase evolution in this scheme, incorporate it into a modified waveform template in Sec. IV, taking the waveform to be the sum of harmonics of the orbital phase, compute the Fourier transformed waveform including alternative theory parameters and compare it with the ppE formalism in sec. V. In Sec. VI we review the Fisher information formalism in order to estimate the errors on the parameters. In sec. VII we explain the details of the Monte Carlo simulations we carried out. We discuss the resulting error distributions on selected parameters in Sec. VIII to see to what extent we can measure deviations from the 2PN gravitational wave phase predicted by GR and how strongly the binary parameters are affected by the introduction of six new parameters to the model. We discuss two representative BBH systems in Secs. VIII A) and VIII B). In sec. VIII C we have a closer look at correlations between the newly-introduced parameters. Because systems at higher redshifts experience higher errors, we plot the maximal redshifts for different upper error limits of the alternative theory parameters in Section VIII D. As an example, we calculate the resulting optimal lower bounds on the Compton wavelength of the graviton in Sec. VIII E. We summarize our work and discuss possible extensions in Sec. IX. In Appendix A we discuss the breakdown of three approximations used in this work and where the integrations should be stopped. The expressions we used for the 2.5PN and 3PN frequency evolution are given in appendix B. We give tables with best-case, worst-case and median measurement errors of both the binary and alternative theory parameters in Appendix C.

II. EVOLUTION OF BLACK HOLE BINARIES WITH PRECESSING SPINS

A complete description of the inspiral evolution of two spinning black holes on a quasi-circular orbit with two individual masses $m_{1,2}$ and the corresponding spin vectors $\boldsymbol{S}_{1,2}(t)$ is given by the angular momentum unit vector $\hat{\boldsymbol{L}}(t)$, the orbital angular frequency $\omega(t)$ and an initial value for the orbital phase $\varphi(t_0)$. Further characteristics such as the orbital separation can be related to ω using post-Newtonian expressions. Therefore a quasi-circular BBH inspiral can be described by 12 intrinsic parameters. In order to relate the binary with a detector, a unit vector $\hat{\boldsymbol{n}}$ pointing from the detector to the barycenter, and a luminosity distance d_L between the two can be introduced, bringing an additional set of 3 extrinsic parameters into play. Thus, to describe a BBH inspiral on quasi-circular orbit, 15 parameters are required.

Since a description of the motion of such a system with full General Relativity is only possible with numerical methods and at high computational cost, an analytic expansion of the Einstein equations in powers of v/c has been studied: the post-Newtonian (PN) formalism. Currently, the equations of motion for spinning objects are known up to 2.5PN, while spin-spin and spin-orbit coupling terms are only known up to 2PN [21]. Therefore we take all the relevant expressions up to 2PN, i.e. $\mathcal{O}[(v/c)^4]$ away from leading order. The evolution equation for the angular frequency of a BBH system is [22]

$$\begin{aligned}\frac{dx}{dt} = \frac{64\nu}{5}\frac{c^3}{GM}x^5\Bigg[1 - \left(\frac{743}{336}+\frac{11\nu}{4}\right)x \\ + \left(4\pi - \frac{1}{12}\beta(113,75)\right)x^{3/2} \\ + \left(\frac{34103}{18144}+\frac{13661\nu}{2016}+\frac{59\nu^2}{18}-\frac{1}{48}\sigma(247,721)\right)x^2\Bigg],\end{aligned} \tag{1}$$

where

$$x \equiv \left(\frac{GM\omega}{c^3}\right)^{2/3} \tag{2}$$

is the dimensionless orbital frequency parameter, $M = m_1 + m_2$ is the total mass and $\nu = m_1 m_2/M^2$ is the symmetric mass ratio. The spin-orbit and spin-spin couplings are given by

$$\beta(a,b) = \frac{c}{G}\sum_{i=1}^{2}\left(\frac{a}{M^2}+\frac{b\nu}{m_i^2}\right)\boldsymbol{S}_i\cdot\hat{\boldsymbol{L}}, \tag{3}$$

and

$$\sigma(a,b) = \frac{c^2}{\nu M^4 G^2}(a\ \boldsymbol{S}_1\cdot\boldsymbol{S}_2 - b(\boldsymbol{S}_1\cdot\hat{\boldsymbol{L}})(\boldsymbol{S}_2\cdot\hat{\boldsymbol{L}})), \tag{4}$$

respectively. The precession of $\hat{\boldsymbol{L}}$ and $\boldsymbol{S}_{1,2}$ induces a time dependence for these couplings, and thus a modulation of the gravitational wave phase. The orbit-averaged evolution equations without radiation reaction ($\dot{\boldsymbol{L}} + \dot{\boldsymbol{S}}_{\boldsymbol{1}} + \dot{\boldsymbol{S}}_{\boldsymbol{2}} = 0$) at 2PN order are [23]

$$\begin{aligned}\dot{\boldsymbol{L}} &= \tfrac{G}{c^2}\tfrac{1}{r^3}\left(\left(2+\tfrac{3m_2}{2m_1}\right)\boldsymbol{S}_1 + \left(2+\tfrac{3m_1}{2m_2}\right)\boldsymbol{S}_2\right)\times\boldsymbol{L} \\ &\quad - \tfrac{3G}{2c^2}\tfrac{1}{r^3}\left(\left(\boldsymbol{S}_2\cdot\hat{\boldsymbol{L}}\right)\boldsymbol{S}_1 + \left(\boldsymbol{S}_1\cdot\hat{\boldsymbol{L}}\right)\boldsymbol{S}_2\right)\times\hat{\boldsymbol{L}}, \qquad (5)\\ \dot{\boldsymbol{S}}_i &= \tfrac{G}{c^2}\tfrac{1}{r^3}\left[\left(2+\tfrac{3m_j}{2m_i}\right)\boldsymbol{L} + \tfrac{1}{2}\boldsymbol{S}_j - \tfrac{3}{2}\left(\boldsymbol{S}_j\cdot\hat{\boldsymbol{L}}\right)\hat{\boldsymbol{L}}\right]\times\boldsymbol{S}_i, \qquad (6)\end{aligned}$$

with $i \neq j$ and $i,j \in \{1,2\}$. The orbital separation r and the angular momentum are related to the orbital frequency by the Newtonian relations

$$L = \mu\left(\frac{G^2M^2}{\omega}\right)^{1/3}, \tag{7}$$

$$r = \left(\frac{GM}{\omega^2}\right)^{1/3}, \tag{8}$$

since higher-order corrections would exceed the 2PN order. Eqs. (1) and (7) enable us to express the evolution equations (6) in terms of the frequency ω:

$$\frac{d\boldsymbol{S}_i}{d\omega} = \frac{5}{96}\frac{c^3}{GM}\omega^{-2}\Bigg[\hat{\boldsymbol{L}}\times\boldsymbol{\Sigma}_i + \frac{1}{2L}\left(\boldsymbol{S}_j - 3\left(\boldsymbol{S}_j\cdot\hat{\boldsymbol{L}}\right)\hat{\boldsymbol{L}}\right)\times\boldsymbol{S}_i\Bigg], \tag{9}$$

$$\frac{d\hat{\boldsymbol{L}}}{d\omega} = \frac{5}{96}\frac{c^3}{GM}\omega^{-2}\frac{1}{L}\left[\boldsymbol{\Sigma}_1+\boldsymbol{\Sigma}_2-\frac{3}{2L}\left(\boldsymbol{\sigma}_1+\boldsymbol{\sigma}_2\right)\right]\times\hat{\boldsymbol{L}} \tag{10}$$

$$= -\frac{1}{L}\left(\frac{d\boldsymbol{S}_1}{d\omega}+\frac{d\boldsymbol{S}_2}{d\omega}\right),$$

with

$$\boldsymbol{\Sigma}_i = \left(2+\frac{3m_j}{2m_i}\right)\boldsymbol{S}_i, \tag{11}$$

and

$$\boldsymbol{\sigma}_i = \left(\boldsymbol{S}_j\cdot\hat{\boldsymbol{L}}\right)\boldsymbol{S}_i. \tag{12}$$

We express the gravitational wave phase in terms of the "principal + direction" [24] defined as the direction of the vector $\hat{\boldsymbol{L}}\times\hat{\boldsymbol{n}}$. A precession of the angular momentum vector changes the principal + direction. The resulting modulation of the gravitational waveform can be expressed by modifying the phase by

$$\delta\varphi = -\int_t^{t_c}\frac{\hat{\boldsymbol{L}}\cdot\hat{\boldsymbol{n}}}{1-\left(\hat{\boldsymbol{L}}\cdot\hat{\boldsymbol{n}}\right)^2}\left(\hat{\boldsymbol{L}}\times\hat{\boldsymbol{n}}\right)\cdot\dot{\hat{\boldsymbol{L}}}\,dt = \delta\varphi_0 + \int_{\omega_0}^{\omega}\frac{\hat{\boldsymbol{L}}\cdot\hat{\boldsymbol{n}}}{1-\left(\hat{\boldsymbol{L}}\cdot\hat{\boldsymbol{n}}\right)^2}\left(\hat{\boldsymbol{L}}\times\hat{\boldsymbol{n}}\right)\cdot\frac{d\hat{\boldsymbol{L}}}{d\omega}\,d\omega, \tag{13}$$

where ω_0 is the orbital frequency at time t_0, $\delta\varphi_0 = -\int_{t_0}^{t_c}(d\delta\varphi/dt)dt$, and $d\hat{\boldsymbol{L}}/d\omega$ is given in Eq. (10). The resulting 2PN orbital phase is then, expressed in terms of the orbital angular frequency: $\phi(\omega)=\varphi(\omega)+\delta\varphi(\omega)$.

A signal observed from a BBH at cosmological distance is redshifted, i.e. the observed frequency is $f_{\rm o} = f_{\rm e}/(1+z)$, where f_e is the frequency of the gravitational waves emitted by the binary. The relation between redshift and luminosity distance in a ΛCDM cosmology without radiation and with $\Omega_\Lambda = 0.72$, $\Omega_m = 0.28$ and $H_0 = 70.1$ km/s/Mpc [25] is

$$d_L(z) = (1+z)\frac{c}{H_0}\int_0^z\frac{dz'}{\sqrt{\Omega_m(1+z')^3+\Omega_\Lambda}}. \tag{14}$$

For binaries at cosmological distance, the redshifted signal can be expressed as one coming from a binary with 'redshifted' masses $\tilde{m}_{1,2} = (1+z)\,m_{1,2}$ at luminosity distance $d_L(z)$. Unfortunately, for gravitational wave experiments, it is not possible to disentangle redshift, mass and distance: only two parameters out of these three can be inferred. Simultaneous observations of electromagnetic counterparts, through which the actual redshift could be measured, could break this correlation and lead to interesting astrophysical insights.

III. MODIFICATIONS TO THE 2PN ORBITAL PHASE

Matched filtering techniques are more sensitive to the gravitational wave phase than to the amplitude. The signal from a BBH inspiral can be described as a sum of harmonics of its orbital phase; to find the imprints of alternative gravity theories on gravitational waves it is therefore reasonable to look at how the orbital phase evolution of a BBH changes for small departures from GR. In the 2PN expansion, the orbital phase evolution can be found by integrating the frequency evolution equation (see Eq. (1) for the PN coefficients b_i)

$$\frac{dx}{dt} = \frac{64\nu}{5}\frac{c^3}{GM}x^5\left[1+b_1x+b_{3/2}x^{3/2}+b_2x^2\right]. \tag{15}$$

As thoroughly discussed by Yunes and Pretorius in the derivation of their ppE formalism [8], in the adiabatic approximation the dimensionless frequency can be expressed as

$$\frac{dx}{dt} = \frac{\dot{E}}{dE/dx}. \tag{16}$$

E is the total binding energy or Hamiltonian (conservative part) of the system while $\dot{E}$ stands for the energy loss through gravitational waves or other physical degrees of freedom of energy loss (dissipative part). Considering the impact of alternative theories on these two quantities leads to modifications of the gravitational wave phase. Certain theories such as Brans-Dicke theory introduce scalar fields which lead to a difference in the self-gravitational binding energy $\mathcal{G}$ per unit mass [26], producing additional dipole radiation. The energy loss formula including dipole contributions can be expressed to leading quadrupole order as [8, 26, 27]:

$$\dot{E} = -\frac{\mu^2G^3M^2}{c^5r^4}\left[\frac{8}{15}(\kappa_1v^2-\kappa_2\dot{r}^2)+\frac{1}{3}\kappa_D\mathcal{G}^2\right]-\mathcal{L}_{\rm other}. \tag{17}$$

Here, v and r are the orbital velocity and separation of the system, respectively, while κ_1 and κ_2 are so-called Peter-Mathews parameters and κ_D is a coefficient for the dipole contribution. $\mathcal{L}_{\rm other}$ stands for any other energy loss channel, either through other polarizations or as yet unknown physical processes. Since we do not

have any good parametrization for $\mathcal{L}_{\rm other}$ so far, we do not consider it. In terms of dimensionless frequency, the dipole radiation term in Eq. (17) leads to an additional x^{-1} term in the PN expansion (15).

We introduce a general parametrization where the effects on the phase are emphasized and no corrections to the wave amplitude are considered. The calculations are done for quasi-circular binaries with precession of both black hole spins described by the full 2PN waveform (2PN expansion of both the phase and the amplitude). We start by introducing corrections to the 2PN orbital frequency evolution dx/dt which will lead to a corrected version of the 2PN orbital phase. To do that, we introduce a correction term a_i for every 2PN coefficient b_i and an additional x^{-1} and $x^{1/2}$ term. Products of a correction term $a_{-1}x^{-1}$ with a PN expanded expression such as $1 + b_1 x + b_{3/2}x^{3/2} + b_2 x^2$ result in b_2 featuring already at 1PN order. Hence for the final result to be consistent at 2PN order, we need to do all the calculations up to 3PN, truncating at 2PN only at the very end. The current 2.5PN expansion accounts for spin-orbit effects while the 3PN expansion does not consider spin effects at all. Nevertheless, these higher order expansions can be used as approximations. The 3PN evolution equations of the dimensionless orbital angular frequency are, motivated from [22, 28] (see appendix B)

$$\begin{aligned}\left(\frac{dx}{dt}\right)_{\rm 3PN} &= \frac{64\nu}{5}\frac{c^3}{GM}x^5\Big[1 + b_1 x + b_{3/2}x^{3/2} + b_2 x^2 \\ &\quad + b_{5/2}x^{5/2} + b_3 x^3 + b_{3,\log}x^3\log(x)\Big]\ ,\end{aligned} \tag{18}$$

with

$$\begin{aligned}b_1 &= -\left(\frac{743}{336} + \frac{11\nu}{4}\right)\ ,\\ b_{3/2} &= \left(4\pi - \frac{1}{12}\beta(113,75)\right)\ ,\\ b_2 &= \left(\frac{34103}{18144} + \frac{13661\nu}{2016} + \frac{59\nu^2}{18} - \frac{1}{48}\sigma(247,721)\right)\ ,\\ b_{5/2} &= \pi\left(-\frac{4159}{672} - \frac{189\nu}{8}\right) + \frac{1}{c}\left(-\frac{40127}{1008} + \frac{1465\nu}{28}\right)\\ &\quad \times\beta(1,0) + \frac{1}{c}\left(-\frac{583}{42} + \frac{3049\nu}{168}\right)\beta(-1,1)\ ,\\ b_3 &= \frac{16447322263}{139708800} - \frac{1712\gamma_e}{105} + \frac{16\pi^2}{3} - \frac{56198689\nu}{217728}\\ &\quad + \frac{451\pi^2\nu}{48} + \frac{541\nu^2}{896} - \frac{5605\nu^3}{2592} - \frac{856}{105}\log(16),\\ b_{3,\log} &= -\frac{856}{105},\end{aligned} \tag{19}$$

where β and σ are the spin-orbit and spin-spin couplings, respectively. To account for alternative theories, we generalize the frequency evolution to

$$\begin{aligned}\left(\frac{dx}{dt}\right)_{\rm mod} &= \left(\frac{dx}{dt}\right)_{\rm 3PN} + \frac{64\nu}{5}\frac{c^3}{GM}x^5\\ &\quad\times\Big[a_{-1}x^{-1} + a_0 + a_{1/2}x^{1/2} + a_1 x\\ &\quad + a_{3/2}x^{3/2} + a_2 x^2 + a_{2,\log}\,x^2\log(x)\Big]\ ,\end{aligned} \tag{20}$$

including corrections to every existing PN parameter and an additional x^{-1} and $x^{1/2}$ term. The reason why $x^2\log(x)$ appears is that a term proportional to $x^3\log(x)$ enters the 3PN phase which has to be included in 2PN corrections because of couplings with x^{-1} terms.

Note that we treat the a_i as constants, i.e. we disregard any dependencies on binary parameters such as masses and spins, since we do not know how they look like in general.

We now follow the steps for the derivation of the gravitational waveform presented in [29], introducing these additional corrections, keeping them at first order, and truncating at 3PN.

By inverting and integrating Eq. (20) we find the time $t(x)$ as a function of the frequency to be of the form:

$$\begin{aligned}t - t_c &\approx t(x)\big|_{\rm 3PN} - t_c - \frac{5}{256\nu}\frac{GM}{c^3}\left[T_{-1}x^{-1} + T_0\right.\\ &\quad + T_{1/2}x^{1/2} + T_1 x + T_{3/2}x^{3/2} + T_2 x^2\\ &\quad \left. + T_{2,\log}x^2\log(x)\right].\end{aligned} \tag{21}$$

The coefficients T_i are functions of a_i. To find the orbital phase as function of frequency, we need to recast $t(x)$ into a series expansion for $x(t)$; we are then able to find the phase by integrating $\omega \propto x^{3/2}$ over time:

$$\begin{aligned}[\varphi(x)]_{\rm mod} &= [\varphi(x)]_{\rm 2PN} + \frac{1}{32\nu}\frac{c^3}{GM}x^{-5/2}\left[A_{-1}x^{-1}\right.\\ &\quad + A_0 + A_{1/2}x^{1/2} + A_1 x + A_{3/2}x^{3/2}\\ &\quad \left. + A_2 x^2 + A_{2,\log}x^2\log(x)\right],\end{aligned} \tag{22}$$

with the phase corrections $A_i(\{a_k\})$ as functions of the orbital frequency evolution corrections introduced in eq. (20). At this point we choose not to consider the correction term $A_{2,log}$ in our implementation for simplicity and thus set $A_{2,log} = 0$ in the following.

IV. MODIFICATIONS TO THE 2PN WAVEFORM

Having found a 2PN expression for the orbital phase corrections, we are able to construct the gravitational

waveform as a series of harmonics of the orbital frequency:

$$h_{+,\times} = \frac{2GM\nu x}{D_L c^2}\left[\sum_{n\geq 0}\left(A^{(n)}_{+,\times}\cos(n\phi) + B^{(n)}_{+,\times}\sin(n\phi)\right)\right]. \tag{23}$$

Here, ϕ is the orbital phase of the binary with spin precession included: $\phi(t) = [\varphi(t)]_{mod} + \delta\varphi(t)$. The coefficients $A^{(n)}_{+,\times}$, $B^{(n)}_{+,\times}$ are both post-Newtonian series in x:

$$A^{(n)}_{+,\times} = \sum_{i\geq 0} a^{(n,i/2)}_{+,\times} x^{i/2}, \qquad B^{(n)}_{+,\times} = \sum_{i\geq 0} b^{(n,i/2)}_{+,\times} x^{i/2}. \tag{24}$$

Explicit expressions for $A^{(n)}_{+,\times}$ and $B^{(n)}_{+,\times}$ can be found in [29]. A three arm classic LISA will form two different detectors with uncorrelated noise: for a detector k with antenna pattern functions F^+_k and $F^\times_k$, the response function can be written in the low frequency approximation (LFA) as

$$\begin{aligned} h_k &= \frac{\sqrt{3}}{2}\left(F^+_k h_+ + F^\times_k h_\times\right) \\ &= \frac{\sqrt{3}GM\nu x}{D_L c^2}\sum_{n\geq 0}\left[A_{k,n}\cos(n\psi) + B_{k,n}\sin(n\psi)\right], \end{aligned} \tag{25}$$

with the antenna pattern functions

$$\begin{aligned} F^+_1(\theta_N,\phi_N,\psi_N) &= \frac{1}{2}\left(1+\cos^2\theta_N\right)\cos 2\phi_N\cos 2\psi_N \\ &\quad - \cos\theta_N \sin 2\phi_N \sin 2\psi_N, \qquad (26)\\ F^\times_1(\theta_N,\phi_N,\psi_N) &= F^+_1(\theta_N,\phi_N,\psi_N - \pi/4), \qquad (27)\\ F^+_2(\theta_N,\phi_N,\psi_N) &= F^+_1(\theta_N,\phi_N - \pi/4,\psi_N), \qquad (28)\\ F^\times_2(\theta_N,\phi_N,\psi_N) &= F^+_1(\theta_N,\phi_N - \pi/4,\psi_N - \pi/4). \qquad (29) \end{aligned}$$

θ_N and ϕ_N are the spherical angles of the position of the binary in the detector frame, and ψ_N is defined through

$$\tan\psi_N \equiv \frac{\hat{\boldsymbol{L}}\cdot\hat{\boldsymbol{z}} - (\hat{\boldsymbol{L}}\cdot\hat{\boldsymbol{n}})(\hat{\boldsymbol{z}}\cdot\hat{\boldsymbol{n}})}{\hat{\boldsymbol{n}}\cdot(\hat{\boldsymbol{L}}\times\hat{\boldsymbol{z}})}, \tag{30}$$

with $\psi = [\varphi]_{mod} + \delta\varphi + \phi_D$, including the LISA Doppler phase $\phi_D(t) = (\omega R/c)\sin\bar{\theta}_N\cos(\bar{\Phi}(t) - \bar{\phi}_N)$, where $R =$ 1 AU and $\bar{\phi}(t) = 2\pi t/1$ yr as explained in [29]. The harmonic coefficients are

$$\begin{aligned} A_{k,n} &= \sum_{i\geq 0}\left(F^+_k a^{(n,i/2)}_+ + F^\times_k a^{(n,i/2)}_\times\right)x^{i/2}, \\ B_{k,n} &= \sum_{i\geq 0}\left(F^+_k b^{(n,i/2)}_+ + F^\times_k b^{(n,i/2)}_\times\right)x^{i/2}\ . \end{aligned} \tag{31}$$

By changing the cosine+sine representation into a cosine+phase representation, we can write Eq. (25) as

$$\begin{aligned} h_k &= \frac{\sqrt{3}GM\nu x}{D_L c^2}\left[A^{(0)}_+ F^+_k + A^{(0)}_\times F^\times_k \right. \\ &\quad \left. + \sum_{n\geq 1} A^{\rm pol}_{k,n}\cos\left(n\psi + \phi^{\rm pol}_{k,n}\right)\right], \end{aligned} \tag{32}$$

with

$$\tan\phi^{\rm pol}_{k,n} = -\frac{B_{k,n}}{A_{k,n}}, \qquad A^{\rm pol}_{k,n} = {\rm sgn}(A_{k,n})\sqrt{A^2_{k,n} + B^2_{k,n}}\ . \tag{33}$$

The Fourier transform of the response function is then, writing the cosine as an exponential and defining the new phase $\psi_{k,n} \equiv n([\varphi]_{mod} + \delta\varphi + \phi_D) + \phi^{\rm pol}_{k,n}$:

$$\begin{aligned} \tilde{h}_k(f) &= \frac{\sqrt{3}GM\nu}{2D_L c^2}\int_{-\infty}^{\infty}\left(\sum_{n\geq 1} x A^{\rm pol}_{k,n}\left[e^{i(2\pi ft - \psi_{k,n})}\right.\right. \\ &\quad \left. + e^{i(2\pi ft + \psi_{k,n})}\right] + 2x\left(A^{(0)}_+ F^+_k + A^{(0)}_\times F^\times_k\right) \\ &\quad \left.\times e^{2\pi i ft}\right)dt\ . \end{aligned} \tag{34}$$

The $n = 0$ integral accumulates around frequencies different from the gravitational wave frequency and $e^{i(2\pi ft + \psi_{k,n})}$ around negative frequencies, so both can be neglected. Then the Fourier transform reduces to

$$\tilde{h}_k(f) = \frac{\sqrt{3}GM\nu}{2D_L c^2}\sum_{n\geq 1}\left[\int_{-\infty}^{\infty} x A^{\rm pol}_{k,n} e^{i(2\pi ft - \psi_{k,n})}dt\right]\ . \tag{35}$$

In the stationary phase approximation (SPA, see e.g. [30, 31]), $\tilde{h}_k(f)$ is approximated by

$$\begin{aligned} \tilde{h}_k(f) &\sim \frac{\sqrt{6\pi}GM\nu}{4D_L c^2}\sum_{n\geq 1} x(t_n) A^{\rm pol}_{k,n}(t_n)\, e^{i(2\pi f t_n - \psi_{k,n} - \frac{\pi}{4})} \\ &\quad \times\sqrt{\frac{1}{\left|\frac{d^2\psi_{k,n}}{dt^2}\right|}}, \end{aligned} \tag{36}$$

evaluated at the stationary points $t_n = t_{\rm 2PN}(f/n)$. The square root of the reciprocal of the second derivative of $\psi_{k,n}$ is found to be

$$\sqrt{\frac{1}{\left|\frac{d^2\psi_{k,n}}{dt^2}\right|}} = \frac{\sqrt{5}\ GM}{4\sqrt{6\nu}\ c^3 x^{11/4}}[S(f)]_{\rm mod}\ , \tag{37}$$

with $[S(f/n)]_{\rm mod} = S_{\rm 2PN}(f/n) + \Delta S$ being a 2PN function with

$$\begin{aligned} S_{\rm 2PN}(f) &= \left[1 + \left(\frac{743}{336} + \frac{11\nu}{8}\right)x + \left(\frac{1}{24}\beta(113,75) \right.\right. \\ &\left. -2\pi\right) x^{3/2} + \left(\frac{7266251}{8128512} + \frac{18913\nu}{16128} + \frac{1379\nu^2}{1152}\right. \\ &\left.\left. + \frac{1}{96}\sigma(247,721)\right) x^2\right], \\ \Delta S &= S_{\text{-}1}x^{-1} + S_0 + S_{1/2}x^{1/2} + S_1 x + S_{3/2}x^{3/2} \\ &+ S_2 x^2 + S_{2,\log}x^2\log(x). \end{aligned} \tag{38}$$

The S_i are functions of the orbital phase corrections A_i. The waveform can then be written as

$$\begin{aligned} \tilde{h}_k(f) \sim\ & \frac{\sqrt{5\pi\nu}G^2M^2}{8D_Lc^5}\sum_{n\geq 1} A^{\rm pol}_{k,n}(t(f/n))x_n^{-7/4}[S(f/n)]_{\rm mod} \\ & \times \exp\left\{i[n([\Psi(f/n)]_{\rm mod} - \delta\varphi(f/n) \right. \\ & \left. - \phi_D[t(f/n)]) - \phi^{\rm pol}_{k,n}[t(f/n)]]\right\}, \end{aligned} \tag{39}$$

where the modified phase is defined as $[\Psi(f/n)]_{\rm mod} = [\Psi(f/n)]_{\rm 2PN} + \Delta\Psi$, with

$$\begin{aligned} \Psi_{\rm 2PN} &= \left(\frac{t_c c^3}{GM}\right)x^{3/2} - \phi_c - \frac{\pi}{4} \\ &+ \frac{3x^{-5/2}}{256\nu}\left[1 + \left(\frac{3715}{756} + \frac{55\nu}{9}\right)x + \left(\frac{1}{3}\beta(113,75)\right.\right. \\ &\left. -16\pi\right)x^{3/2} + \left(\frac{15293365}{508032} + \frac{27145\nu}{504} + \frac{3085\nu^2}{72}\right. \\ &\left.\left. + \frac{5}{24}\sigma(247,721)\right)x^2\right], \\ \Delta\Psi &= \frac{3}{256\nu}x^{-5/2}\left(\Psi_{\text{-}1}x^{-1} + \Psi_0 + \Psi_{1/2}x^{1/2} + \Psi_1 x \right. \\ &\left. + \Psi_{3/2}x^{3/2} + \Psi_2 x^2\right). \end{aligned} \tag{40}$$

The Ψ_i are also functions of the orbital phase corrections A_i. It makes thus sense to work only with the phase correction parameters Ψ_i from now on. The coefficients of ΔS are then, given as functions of Ψ_i:

$$\begin{aligned} S_{\text{-}1} &= -\frac{7}{24}\Psi_{\text{-}1}\ , \\ S_0 &= -\frac{35}{48}b_1\Psi_{\text{-}1} - \frac{1}{2}\Psi_0\ , \\ S_{1/2} &= -\frac{49}{48}b_{3/2}\Psi_{\text{-}1} - \frac{7}{15}\Psi_{1/2}\ , \\ S_1 &= -\frac{21}{16}\left(\frac{b_1^2}{4} - b_2\right)\Psi_{\text{-}1} + -\frac{7}{12}b_1\Psi_0 - \frac{3}{8}\Psi_1\ , \\ S_{3/2} &= \left(\frac{77}{96}b_1b_{3/2} - \frac{49}{24}b_{5/2}\right)\Psi_{\text{-}1} - \frac{3}{4}b_{3/2}\Psi_0 \\ &- \frac{7}{15}b_1\Psi_{1/2} - \frac{1}{4}\Psi_{3/2}\ , \\ S_2 &= \left(-\frac{91}{384}b_1^3 + \frac{91}{96}b_1b_2 - \frac{7}{3}b_3 + \frac{91}{192}b_{3/2}^2\right. \\ &\left. - \frac{7}{12}b_{3,\log}\right)\Psi_{\text{-}1} + \left(\frac{11}{48}b_1^2 - \frac{11}{12}b_2\right) \\ &\Psi_0 - \frac{7}{12}b_{3/2}\Psi_{1/2} - \frac{27}{80}b_1\Psi_1 - \frac{7}{60}\Psi_2\ , \\ S_{2,\log} &= -\frac{7}{3}b_{3,\log}\Psi_{\text{-}1}\ . \end{aligned} \tag{41}$$

All the alternative theory parameters Ψ_i are treated as constants. They will most probably depend on other binary parameters such as masses and spins, but it is not possible at this point to find a general parametrization in terms of binary parameters. In practice this could lead to further covariances between the alternative theory and binary parameters. Since in the PN expansion of the gravitational wave phase usually coefficients depending on the symmetric mass ratio of the form $\alpha_1 + \alpha_2\nu + \alpha_3\nu^2 + \ldots$ appear, one could theoretically introduce a new set of parameters, as an attempt to disentangle binary and alternative theory parameters, but it would increase the number of parameters drastically, therefore reducing the accuracy of a single measurement. Since such a parametrization would not induce time varying couplings, and this study focuses on the measurement accuracy for individual systems, we chose not to take the mass ratio into account. However, the spins might lead to time varying modifications; we chose not to take them into account either, because of the lack of theoretical predictions for their form.

V. CONNECTION TO THE PPE FORMALISM

The idea of this work is based on the ppE formalism by Yunes and Pretorius [8]. To look for deviations from GR, they introduce modifications to the amplitude and phase of the gravitational wave in the frequency domain [20]:

$$A(f) = \left(1+\sum_k \alpha_k\, u^{a_k}\right) A^{\rm GR}(f),$$
$$\Psi(f) = \left(1+\sum_k \beta_k\, u^{b_k}\right) \Psi^{\rm GR}(f). \quad (42)$$

Here, $u = x^{3/2}\nu^{3/5}$ is the reduced frequency and α_k, β_k are alternative theory parameters which could depend on the binary parameters, such as on the symmetric mass ratio or on some spin/angular-momentum quantities. These deviations results in a modification for the n-th harmonic of the gravitational waveform (in the frequency domain) of the form

$$\tilde{h}_n(f) = \tilde{h}_n^{\rm GR}(f)\,[1+\Delta A_n(f/n)]\, e^{in\Delta\Psi(f/n)}, \quad (43)$$

where ΔA_n and $\Delta\Psi$ are power series in the frequency arising from the above modifications, and the overall waveform is the sum $\tilde{h}(f) = \sum_n \tilde{h}_n(f)$.

Previous studies [20, 32] used the restricted waveform ($n = 2$) and investigated leading order deviations using a waveform template of the form

$$\tilde{h}(f) = \tilde{h}^{\rm GR}(f)\left[1+\alpha(4\nu)^A u^a\right] e^{i\beta(4\nu)^B u^b}, \quad (44)$$

where a dependency on the symmetric mass ratio ν is introduced. Let us relate this to our parametrization given in eq. (39):

$$\tilde{h}_n(f) = \tilde{h}_n^{\rm GR}(f)\left(1+\frac{\Delta S(f/n)}{S(f/n)}\right) e^{in\Delta\Psi(f/n)}\ . \quad (45)$$

Since in our implementation we start from the frequency evolution (20), the amplitude correction term $\Delta S/S$ entering through the stationary phase approximation is only a pseudo correction, as it can be expressed with phase correction parameters Ψ_i (41). Thus our implementation does not consider real amplitude modifications, only the phase parameters Ψ_i can be put into relation with the ppE formalism. The phase modifications $\Delta\Psi$ are, for the ppE formalism and our implementation respectively:

$$\Delta\Psi_{\rm ppE} = \sum_k \beta_k\,(4\nu)^{B_k}\, u^{b_k},$$
$$\Delta\Psi_{\text{this work}} = \frac{3}{256\nu}\sum_i \Psi_i\, x^{i-5/2}. \quad (46)$$

Because of the special treatment of the symmetric mass ratio prefactor with a parameter B_k and since the symmetric mass ratio enters the conversion between u and x, there is no clear way how to put the parameter sets $\{\beta_k, B_k, b_k\}$ and $\{\Psi_i, i\}$ into relation. Only the frequency powers b_k and i where the corrections enter can be compared: they relate as $b_k = \frac{2}{3}(i_k - \frac{5}{2})$, where the i_k are our summation indices. Our implementation is thus a subset of the ppE formalism with $b_k = \{-7/3, -5/3, -4/3, -1, -2/3, -1/3\}$.

This subset with fixed frequency does not cover the leading order contributions of every alternative to GR currently proposed. While it is able to catch leading order deviations originating from Brans-Dicke, massive graviton and quadratic curvature-type theories, it will not see the leading order imprints of Dynamical Chern-Simons gravity, Variable $G(t)$ theories and theories including extra dimensions (see [20] for an overview table of the leading order contributions of alternative theories). On the other hand, our implementation is able to investigate next-to-leading order effects and can quantify how the inclusion of alternative theory parameters with more than just one frequency power affects the measurement accuracy of a LISA-type detector, including the effects of spin precession and higher harmonics.

VI. PARAMETER ESTIMATION

To estimate how accurately LISA can measure deviations from the 2PN gravitational wave phase predicted by General Relativity, we use the standard Fisher information formalism for gravitational wave experiments, as reviewed in [33, 34]. The Fisher information formalism holds only in the limit of high SNR; this is true for a LISA-type mission, for which SNRs of a few thousands are expected. For low SNR, advanced Bayesian techniques exploring the whole parameter space such as Markov Chain Monte Carlo methods, (see e.g. [20, 35]) are needed. Also, once data will become available, Bayesian statistics taking into account prior probability distributions will be the preferred framework [36].

We assume the gravitational wave signal to be buried in stationary Gaussian noise $n(t)$ such that the different Fourier components $\tilde{n}(f)$ are uncorrelated. Moreover, we presume that the noise of the two detectors is totally uncorrelated. Assuming flat priors, for a signal $h(t)$ described by a true parameter set $\boldsymbol{\theta}_t$, with noise with spectral density $S_n(f)$, the probability for the measured data $d(t) = n(t) + h(t;\boldsymbol{\theta}_t)$ to take this specific form is proportional to

$$p(d|\boldsymbol{\theta}_t) \propto e^{-(d-h(\boldsymbol{\theta}_t)|d-h(\boldsymbol{\theta}_t))}, \quad (47)$$

where the inner product $(g|h)$ is defined as

$$(g|h) = 4\ Re\int_0^\infty \frac{\tilde{g}^*(f)\tilde{h}(f)}{S_n(f)} df\ . \quad (48)$$

The use of a waveform template with the parameter set $\boldsymbol{\theta}$ is inaccurate by $\Delta\theta^i = \theta^i_t - \theta^i$. The errors $\Delta\theta^i$ are then approximately given by maximizing the above likelihood distribution, expanding it in the errors assumed to be small and keeping only first derivatives [34]:

$$\langle \Delta\theta_i \Delta\theta_j \rangle = \Sigma_{ij} = (\Gamma^{-1})_{ij} + \mathcal{O}\left(\frac{1}{\mathrm{SNR}}\right) \ , \tag{49}$$

where Σ is the covariance matrix and

$$\Gamma_{ij} = \left(\frac{\partial h}{\partial \theta^i} \middle| \frac{\partial h}{\partial \theta^j} \right) \tag{50}$$

is the so-called *Fisher matrix*. The expected measurement errors on the parameters θ^i can be expressed as

$$\Delta\theta^i = \sqrt{(\Gamma^{-1})^{ii}}. \tag{51}$$

We chose the same noise curve for classic LISA as in [29], namely the piecewise fit used by the LISA parameter estimation community [37] given by the instrumental noise

$$\begin{aligned} S_n(f) \ &= \ \frac{1}{L^2}\Bigg\{ \left[1 + \frac{1}{2}\left(\frac{f}{f_*}\right)^2\right] S_p \\ &\quad + \left[1 + \left(\frac{10^{-4}}{f}\right)^2\right] \cdot \frac{4 S_a}{(2\pi f)^4} \Bigg\}, \end{aligned} \tag{52}$$

(53)

and the confusion noise

$$S_{\mathrm{conf}}(f) \ = \begin{cases} 10^{-44.62} f^{-2.3} & (f \leqslant 10^{-3}), \\ 10^{-50.92} f^{-4.4} & (10^{-3} < f \leqslant 10^{-2.7}), \\ 10^{-62.8} f^{-8.8} & (10^{-2.7} < f \leqslant 10^{-2.4}), \\ 10^{-89.68} f^{-20} & (10^{-2.4} < f \leqslant 10^{-2}), \\ 0 & (10^{-2} < f), \end{cases} \tag{54}$$

where $L = 5 \times 10^9$ m is the arm length of classic LISA, $S_p = 4 \times 10^{-22}$ m^2 Hz^{-1} is the white position noise level, $S_a = 9 \times 10^{-30}$ m^2 s^{-4} Hz^{-1} is the white acceleration noise level, and $f_* = c/(2\pi L)$ is the arm transfer frequency. The total noise curve is then $S_h(f) = S_n(f) + S_{\mathrm{conf}}(f)$.

VII. SIMULATIONS

For our simulations, 21 parameters are needed: 15 GR parameters plus 6 alternative theory parameters. We use

(i) $\log_{10} m_1/M_\odot$ and $\log_{10} m_2/M_\odot$, for the masses of the two black holes.

(ii) $\mu_l = \cos\theta_l$ and ϕ_l, for the spherical angles of the orbital angular momentum $\boldsymbol{L}$ at $\gamma = \frac{1}{6}$.

(iii) $\mu_1 = \cos\theta_1$ and ϕ_1 for the spherical angles of the spin of the first black hole $\boldsymbol{S}_1$ at $\gamma = \frac{1}{6}$.

(iv) $\chi_1 = \frac{c}{G m_1^2} |\boldsymbol{S}_1|$ for the dimensionless strength of the spin of the first black hole, which has to satisfy $0 \leqslant \chi_1 < 1$.

(v) $\mu_2 = \cos\theta_2$, ϕ_2, and χ_2 for the second black hole, defined equivalently as for the first one.

(vi) $\log t_c$, for the time of coalescence.

(vii) φ_c, the phase at coalescence. As this phase is random and its determination is not of any astrophysical interest, we can safely neglect constants in the orbital phase, in particular $\delta\varphi_0$ from Eq. (13).

(viii) $\mu_n = \cos\theta_n$ and ϕ_n, the spherical angles of the position of the binary in the sky.

(ix) $\log d_L$, for the luminosity distance between the source and the Solar System.

(x) Ψ_i with $i \in \{-1, 0, 1/2, 1, 3/2, 2\}$, the 6 alternative theory parameters defined in section IV

All angles are taken in the frame tied to the distant stars. Moreover, we set $t = 0$ to be at the time when LISA will start operating.

We perform Monte Carlo simulations, keeping the masses $m_{1,2}$, the redshift z and the alternative theory parameters Ψ_i fixed, and randomizing all other parameters using a flat probability distribution. The spin precession equations (9) are integrated using a fourth order adaptive Runge-Kutta algorithm to find the evolution of $\hat{\boldsymbol{L}}(\omega)$ and $\boldsymbol{S}_{1,2}(\omega)$, going backwards in frequency.

As generic starting point for ω, we chose the frequency at the Schwarzschild ISCO (innermost stable circular orbit) $r_{\mathrm{ISCO}} = 6\,GM/c^2$. Even though such a clear ISCO does not exist for black hole binaries with comparable mass and precessing spins, we find that this limit is a good cut-off criterion, avoiding unphysical results. For more information about our considerations, the reader is referred to section A in the appendix.

We stop the evolution either at $t = 0$ or when the frequency of the highest harmonic goes below the LISA band ($6\omega < 3 \times 10^{-5}$ Hz). The upper and lower bounds on all the randomized parameters of the simulation are straightforward (d_L is just a function of the redshift z, defined in (14)), except for t_c for which we set a lower bound of $t_c = t_{2\mathrm{PN}}(\omega(r = r_{\mathrm{ISCO}}))$ using Eq. (21) and an upper bound of $t_c = 2$yr, which is the minimum science requirement for the LISA mission running time.

Using the angular momentum, spin and orbital time evolution we are able to compute the Fisher matrix elements (50), taking the analytical derivatives with respect to $\log t_c$, $\log d_L$, ϕ_c, μ_n, ϕ_n and all the GR correction parameters Ψ_i. The first three derivatives are easy to compute:

$$\frac{\partial \tilde{h}_k(\theta^j, f)}{\partial \log t_c} = 2\pi i f\, t_c\, \tilde{h}_k(\theta^j, f), \tag{55}$$

$$\frac{\partial \tilde{h}_k(\theta^j, f)}{\partial \log d_L} = -\tilde{h}_k(\theta^j, f), \tag{56}$$

$$\frac{\partial \tilde{h}_k(\theta^j, f)}{\partial \varphi_c} = -i \sum_n n \tilde{h}_{k,n}(\theta^j, f), \tag{57}$$

where $\tilde{h}_{k,n}$ is the nth harmonic of $\tilde{h}_k$. The derivatives with respect to the corrections Ψ_i are of the form

$$\begin{aligned}\frac{\partial \tilde{h}_k}{\partial \Psi_i}(f) \;=\; & \frac{\sqrt{5\pi\nu} G^2 M^2}{8 D_L c^5} \sum_{n\geq 1} A^{\rm pol}_{k,n} x_n^{-7/4} \\ & \times e^{i\left[n(\Psi_{\rm GR}+\Delta\Psi-\delta\varphi-\phi_D)-\phi^{\rm pol}_{k,n}\right]} \\ & \times \left(i\; n\;\; (S_{\rm 2PN}+\Delta S)\, \frac{\partial \Delta\Psi}{\partial \Psi_i} + \frac{\partial \Delta S}{\partial \Psi_i} \right),\end{aligned} \tag{58}$$

and can be calculated in a straightforward way. The derivatives which we could not compute analytically are approximated by

$$\frac{\partial \tilde{h}_k(\theta^j, f)}{\partial \theta^i} \approx \frac{\tilde{h}_k(\theta^j + \epsilon\delta^{ij}/2, f) - \tilde{h}_k(\theta^j - \epsilon\delta^{ij}/2, f)}{\epsilon}, \tag{59}$$

where ϵ is a small displacement of the parameter θ_i which we chose to be of the constant value $\epsilon = 10^{-7}$ for every parameter, except for ϕ_l for which ϵ was divided by $2 - 2|\mu_l|$, μ_i ($i \in \{1, 2\}$) for which ϵ was divided by $5\chi_i$, and ϕ_i for which ϵ was divided by $10\chi_i(1-|\mu_i|)$. The formula is accurate up to $O(\epsilon^2)$.

For each set of parameters we then compute the Fisher matrix using *Clenshaw-Curtis quadrature* and then invert it in order to find the corresponding errors on the parameters which we analyze in section VIII. In order to avoid matrix inversion problems, we use a normalization of the Fisher-Matrix so that all diagonal elements are $A_{ii} = 1$ and all off-diagonal elements are in the range $A_{ij} \in [-1; 1]$:

$$A_{ij} \equiv \frac{1}{\sqrt{\Gamma_{ii}\Gamma_{jj}}}\, \Gamma_{ij}\ . \tag{60}$$

After inversion, the covariance matrix can then be recovered with

$$\Sigma_{ij} = \frac{1}{\sqrt{\Gamma_{ii}\Gamma_{jj}}}\, A^{-1}_{ij}\ . \tag{61}$$

In situations where $\hat{\boldsymbol{L}} \cdot \hat{\boldsymbol{n}}$ is close to 1, the Runge Kutta method fails to converge because

$$\frac{d\delta\varphi}{d\omega} = \frac{\hat{\boldsymbol{L}} \cdot \hat{\boldsymbol{n}}}{1 - \left(\hat{\boldsymbol{L}} \cdot \hat{\boldsymbol{n}}\right)^2} \left(\hat{\boldsymbol{L}} \times \hat{\boldsymbol{n}}\right) \cdot \frac{d\hat{\boldsymbol{L}}}{d\omega} \underset{\hat{\boldsymbol{L}}\cdot\hat{\boldsymbol{n}}\to 1}{\longrightarrow} \infty. \tag{62}$$

Whenever this happens, we take the approximate value

$$\begin{aligned}&\delta\varphi(\omega + \delta\omega) \approx \\ &\delta\varphi(\omega) + \text{angle}\left[\left(\hat{\boldsymbol{L}}(\omega+\delta\omega) \times \hat{\boldsymbol{n}}\right), \left(\hat{\boldsymbol{L}}(\omega) \times \hat{\boldsymbol{n}}\right)\right],\end{aligned} \tag{63}$$

as explained in [29].

VIII. RESULTS

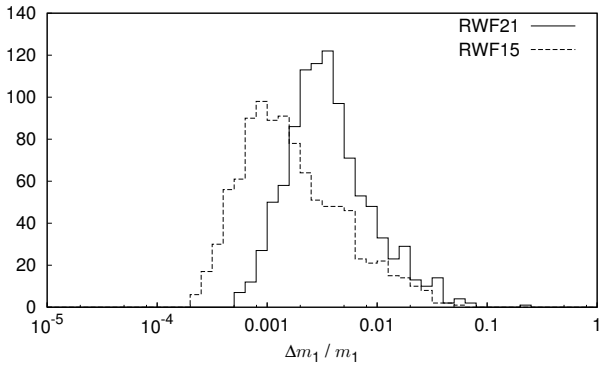

FIG. 1: Comparison between the estimated distributions of the measurement error on m_1 for a low-mass binary system $m_1 = 1 \times 10^6 M_\odot$ and $m_2 = 3 \times 10^5 M_\odot$ with (RWF21) and without (RWF15) including alternative theory parameters, using only the restricted waveform.

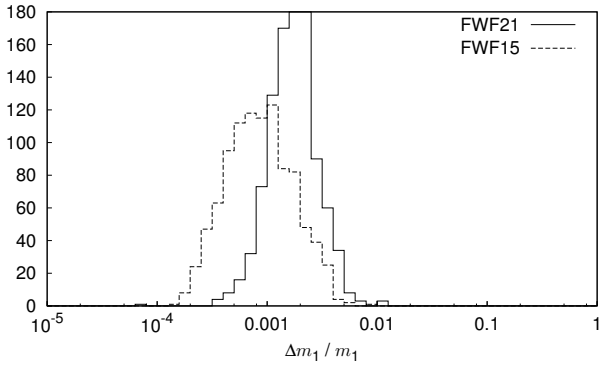

FIG. 2: Comparison between the estimated distributions of the measurement error on m_1 for a low-mass binary system $m_1 = 1 \times 10^6 M_\odot$ and $m_2 = 3 \times 10^5 M_\odot$ with (FWF21) and without (FWF15) including alternative theory parameters and using the full waveform.

We performed simulations for 17 different mass configurations, with total masses between $10^5 M_\odot$ and $10^8 M_\odot$, mass ratios varying between 1:1 and 1:10, and using 10^3 points in the parameter space for each configuration.

The redshift has been kept fixed to $z = 1$ since it is not possible to disentangle redshift, mass and distance. The signal coming from a binary with masses $m_{1,2}$ at redshift z and luminosity distance $d_L(z)$ can be expressed with one from an apparent binary with $\tilde{m}_{1,2} = \frac{1+z}{1+z_0} m_{1,2}$ at redshift z_0 and luminosity distance $d_L(z_0)$ multiplied by an overall factor of $d_L(z_0)/d_L(z)$. Thus every BBH inspiral producing a signal at redshift z can be described with a waveform template at redshift z_0. The Fisher matrix scales as

$$\begin{aligned}\Gamma^{(z)}_{ij} &= \left(\frac{\partial h}{\partial \theta^i}(m_1, m_2, z)\middle|\frac{\partial h}{\partial \theta^j}(m_1, m_2, z)\right) \\ &= \left(\frac{d_L(z_0)}{d_L(z)}\right)^2 \left(\frac{\partial h}{\partial \theta^i}(\tilde{m}_1, \tilde{m}_2, z_0)\middle|\frac{\partial h}{\partial \theta^j}(\tilde{m}_1, \tilde{m}_2, z_0)\right) \\ &= \left(\frac{d_L(z_0)}{d_L(z)}\right)^2 \Gamma^{(z_0)}_{ij}.\end{aligned} \tag{64}$$

The errors on the parameters scale then with

$$\Delta\theta^i(z) = \frac{d_L(z)}{d_L(z_0)} \Delta\theta^i(z_0). \tag{65}$$

Since we choose to work in a picture where General Relativity is the theory assumed to be true and we are keen to know how well LISA will be able to measure deviations from its post-Newtonian expansion terms ψ_i, we fixed the alternative theory parameters to the fiducial values $\Psi_i = 0$.

For each of the 17 binaries we computed the best-case measurement error (5% quantile), the typical error (median) and the worst-case error (95% quantile) for the full (FWF) and restricted waveforms (RWF) and present them in tables I-XIV. For each BBH parameter we are interested in, we give an error table with (21 parameters in total) and without (15 parameters in total) including the alternative theory parameters Ψ_i. We do this to show how much accuracy is lost by introducing alternative theory corrections into a GR waveform template. For binaries where no signal can be extracted from the dataset, we fix the error to infinity.

We give the errors on the sky localization not in terms of errors on μ_n and ϕ_n but instead in terms of an error ellipse with principal axes $2a$ and $2b$, enclosing the region outside of which there is an $1/e$ probability of finding the binary, following [38].

Moreover, in tables XV-XX we give measurement errors on the alternative theory parameters, using both the RWF and FWF.

We roughly divide the binaries into two classes: low-mass binaries ($M \lesssim 10^7 M_\odot$) and high-mass binaries ($M \gtrsim 10^7 M_\odot$). Below we discuss these two cases, using BBHs with $m_1 = 10^6 M_\odot$, $m_2 = 3 \times 10^5 M_\odot$ and $m_1 = 3 \times 10^7 M_\odot$, $m_2 = 10^7 M_\odot$ as representative examples for low-mass and high-mass binaries respectively. We find when using both the RWF and the FWF, the error distributions of the mass and spin parameters behave similarly, losing a factor $1.2 - 5$ of accuracy when alternative theory parameters are included. The error on the sky location of the binary $2a$ and $2b$ is at maximum an order of magnitude worse. For high-mass binaries, factors of ~ 10 and ~ 100 are lost in the determination of the luminosity distance d_L, using the FWF and RWF respectively. While the RWF/FWF errors on the alternative theory parameters are almost equal for low-mass binaries, the RWF errors are about 100 times higher for high-mass binaries

A. Low-mass binaries

For low-mass binaries with total masses below $10^7 M_\odot$ we find that in general, using the FWF instead of the RWF improves the measurement errors $\Delta\Psi_i$ on the alternative theory parameters by a factor of $\sim 1.5 - 3$. The correlation with the new parameters causes a decrease in the accuracy of the 15 binary parameters. For both the FWF and the RWF, the errors on the mass and spin parameters are typically worse by a factor of $2 - 5$ while the luminosity distance is approximately half as accurate. The sky location errors increase only by $\sim 10\%$; this is reasonable, since we do not expect alternative theories to correlate strongly with rotations on a large scale. Therefore it is not necessary to use the FWF instead of the RWF for the sole purpose of measuring alternative gravity parameters in the low-mass regime.

We present selected distributions of the measurement errors $\Delta m_1/m_1$, $\Delta\chi_1/\chi_1$, $2a$, $\Delta d_L/d_L$ and all the six $\Delta\Psi_i$ in figures 1-14. The error distributions of $\Delta m_2/m_2$, $\Delta\chi_2/\chi_2$ and $2b$ are similar to the ones of $\Delta m_1/m_1$, $\Delta\chi_1/\chi_1$ and $2a$.

It is important to recall that we used the low frequency approximation (LFA) [39–42] to generate the LISA detector response. This approximation holds as long as the wavelength of the gravitational wave is much larger than the arm length L of the LISA-type detector, in other words: as long as $f_{GW} \ll f_* = \frac{c}{2\pi L}$, where c is the speed of light and f_* is the so called *transfer frequency*. As soon as the wavelength is comparable to the arm length, the detector response function begins to depend strongly on the sky location and orientation of the source. Effects neglected before, such as the cartwheel motion of LISA, become important, resulting in a modulation of the the waveforms: more information about orientation and sky location is encoded in the signal. Consequently, the errors on extrinsic parameters such as the angles μ_n, ϕ_n, the luminosity distance d_L and the angular momentum orientation μ_l, ϕ_l effectively decrease compared to the LFA, while the intrinsic parameter errors differ only

slighly. Usually, the problems with the approximation start around 3 mHz [41–43]: in our case the first three mass configurations with total masses of 3.3×10^5, 4×10^5 and $6\times10^5 M_\odot$ are above this limit, with frequencies (at $f_{\rm ISCO} = 6\,GM/c^2$ and redshift z=1) of 6.6, 5 and 3.6 mHz, respectively. Following fig. 2 in [41], this means that our results for these three configurations should be too pessimistic, the relative errors on the luminosity distance would in general be smaller by $\sim 10\%$, 20% and 50% for the respective configurations. Also the errors on sky location and angular momentum orientation will be better by up to $\sim 50\%$ for the 3.3×10^5 binary.

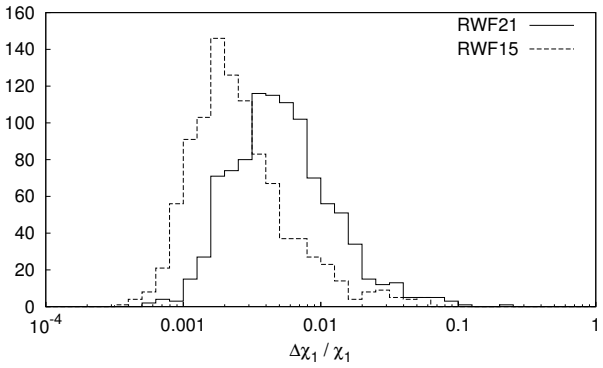

FIG. 3: Comparison between the estimated distributions of the measurement error on χ_1 for a low-mass binary system $m_1 = 1\times10^6 M_\odot$ and $m_2 = 3\times10^5 M_\odot$ with (RWF21) and without (RWF15) including alternative theory parameters, using only the restricted waveform.

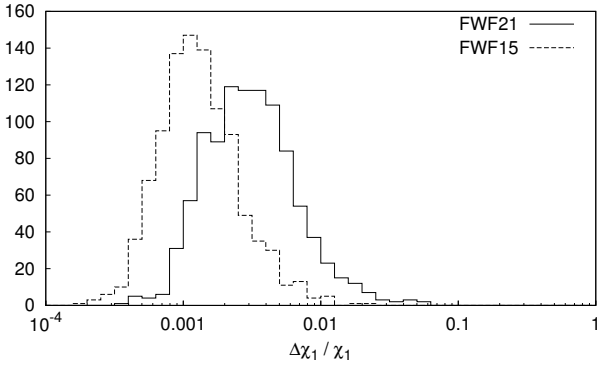

FIG. 4: Comparison between the estimated distributions of the measurement error on χ_1 for a low-mass binary system $m_1 = 1\times10^6 M_\odot$ and $m_2 = 3\times10^5 M_\odot$ with (FWF21) and without (FWF15) including alternative theory parameters and using the full waveform.

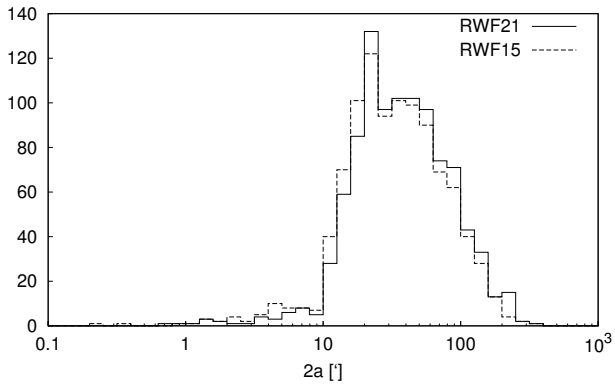

FIG. 5: Comparison between the estimated distributions of the major axis of the positioning error ellipse for a low-mass binary system $m_1 = 1\times10^6 M_\odot$ and $m_2 = 3\times10^5 M_\odot$ with (RWF21) and without (RWF15) including alternative theory parameters, using only the restricted waveform.

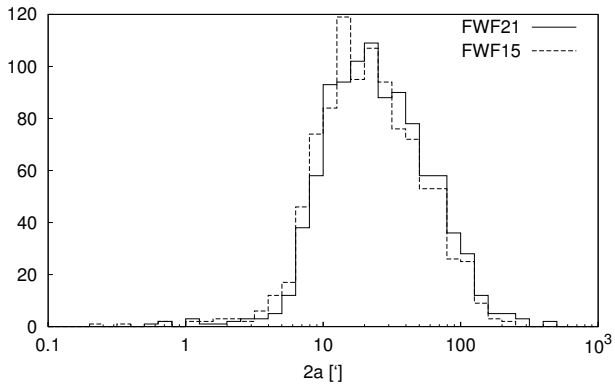

FIG. 6: Comparison between the estimated distributions of the major axis of the positioning error ellipse for a low-mass binary system $m_1 = 1\times10^6 M_\odot$ and $m_2 = 3\times10^5 M_\odot$ with (FWF21) and without (FWF15) including alternative theory parameters and using the full waveform.

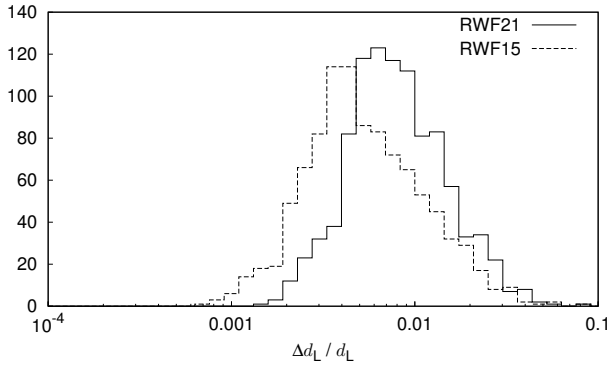

FIG. 7: Comparison between the estimated distributions of the measurement error on d_L for a low-mass binary system $m_1 = 1\times10^6 M_\odot$ and $m_2 = 3\times10^5 M_\odot$ with (RWF21) and without (RWF15) including alternative theory parameters, using only the restricted waveform.

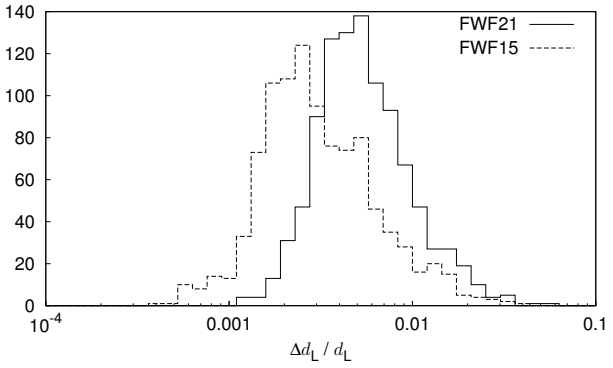

FIG. 8: Comparison between the estimated distributions of the measurement error on d_L for a low-mass binary system $m_1 = 1 \times 10^6 M_\odot$ and $m_2 = 3 \times 10^5 M_\odot$ with (FWF21) and without (FWF15) including alternative theory parameters, using only the restricted waveform.

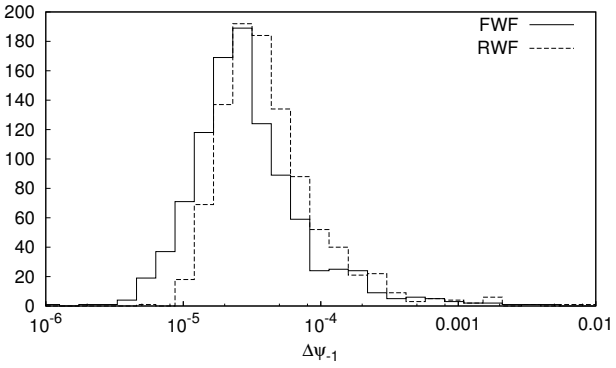

FIG. 9: Comparison between the estimated distributions of the measurement error on the alternative theory parameter Ψ_{-1} for a low-mass binary system $m_1 = 1 \times 10^6 M_\odot$ and $m_2 = 3 \times 10^5 M_\odot$, using the restricted waveform (RWF) and the full waveform (FWF).

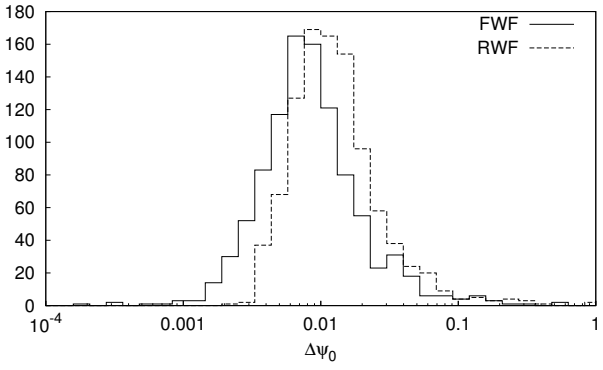

FIG. 10: Comparison between the estimated distributions of the measurement error on the alternative theory parameter Ψ_0 for a low-mass binary system $m_1 = 1 \times 10^6 M_\odot$ and $m_2 = 3 \times 10^5 M_\odot$, using the RWF and the FWF.

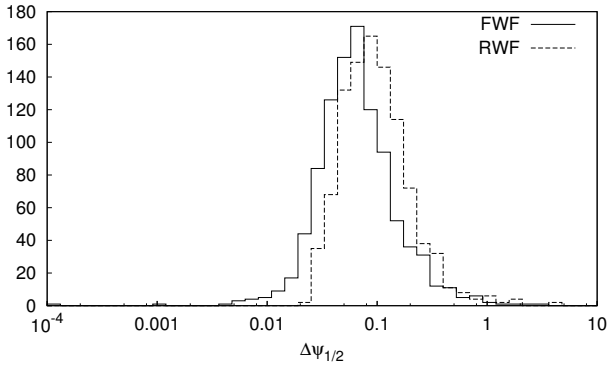

FIG. 11: Comparison between the estimated distributions of the measurement error on the alternative theory parameter $\Psi_{1/2}$ for a low-mass binary system $m_1 = 1 \times 10^6 M_\odot$ and $m_2 = 3 \times 10^5 M_\odot$, using the RWF and the FWF.

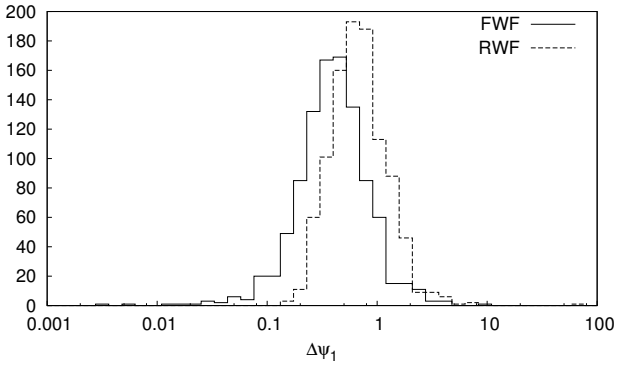

FIG. 12: Comparison between the estimated distributions of the measurement error on the alternative theory parameter Ψ_1 for a low-mass binary system $m_1 = 1 \times 10^6 M_\odot$ and $m_2 = 3 \times 10^5 M_\odot$, using the RWF and the FWF.

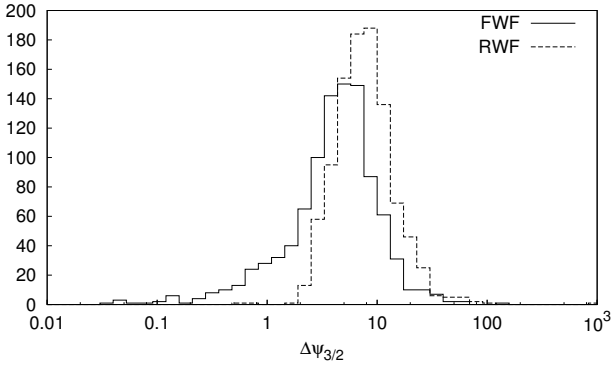

FIG. 13: Comparison between the estimated distributions of the measurement error on the alternative theory parameter $\Psi_{3/2}$ for a low-mass binary system $m_1 = 1 \times 10^6 M_\odot$ and $m_2 = 3 \times 10^5 M_\odot$, using the RWF and the FWF.

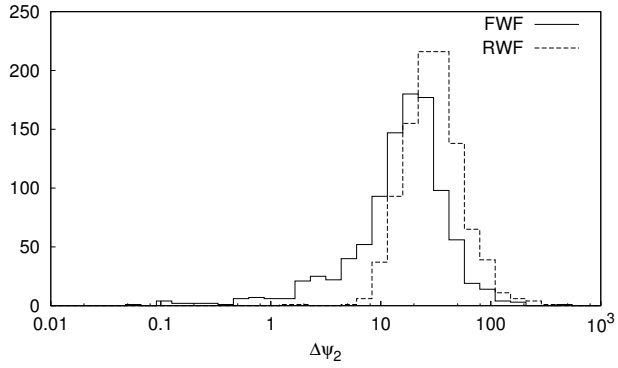

FIG. 14: Comparison between the estimated distributions of the measurement error on the alternative theory parameter Ψ_2 for a low-mass binary system $m_1 = 1 \times 10^6 M_\odot$ and $m_2 = 3 \times 10^5 M_\odot$, using the RWF and the FWF.

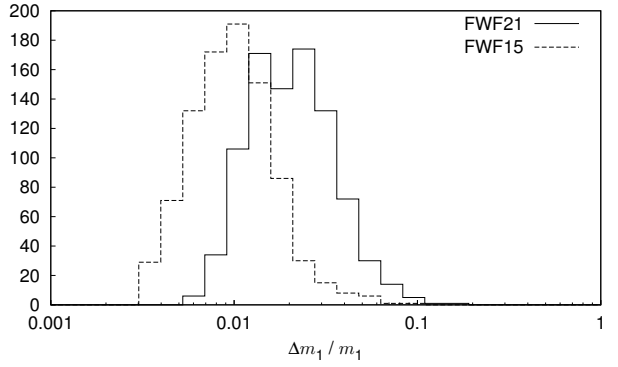

FIG. 15: Comparison between the estimated distributions of the measurement error on m_1 for a high-mass binary system $m_1 = 3 \times 10^7 M_\odot$ and $m_2 = 1 \times 10^7 M_\odot$ with (FWF21) and without (FWF15) including alternative theory parameters and using the full waveform.

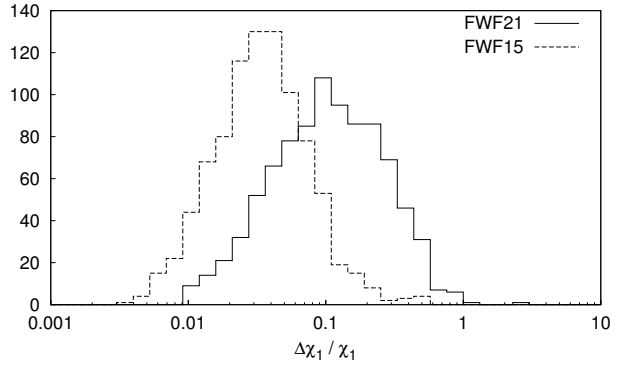

FIG. 16: Comparison between the estimated distributions of the measurement error on χ_1 for a high-mass binary system $m_1 = 3 \times 10^7 M_\odot$ and $m_2 = 1 \times 10^7 M_\odot$ with (FWF21) and without (FWF15) including alternative theory parameters and using the full waveform.

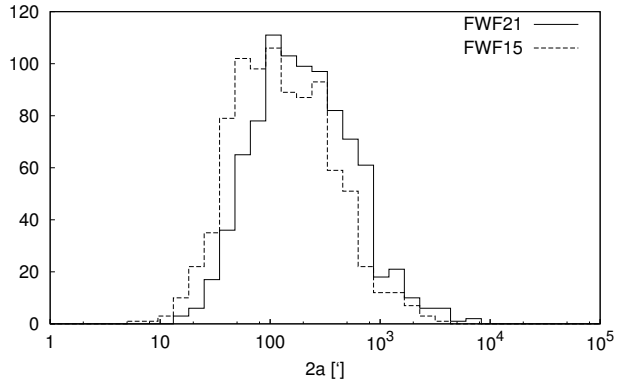

FIG. 17: Comparison between the estimated distributions of the major axis of the positioning error ellipse for a high-mass binary system $m_1 = 3 \times 10^7 M_\odot$ and $m_2 = 1 \times 10^7 M_\odot$ with (FWF21) and without (FWF15) including alternative theory parameters and using the full waveform.

B. High-mass binaries

By using the FWF instead of the RWF for high-mass binaries with total masses $\gtrsim 10^7 M_\odot$, we find significant improvements for the measurement errors of the alternative theory parameters by factors of $\sim 100 - 1000$ for $\Delta\Psi_{-1}$, $\sim 30 - 60$ for $\Delta\Psi_0$ and $\Delta\Psi_{1/2}$, and $\sim 10 - 100$ for $\Delta\Psi_1$, $\Delta\Psi_{3/2}$ and $\Delta\Psi_2$. This makes it clear that it is inevitable to use the FWF in the high-mass regime to perform precision tests of GR. In any case, since the second harmonic spends only a few orbits in the LISA band, the use of the RWF is not trustworthy. Moreover, for BBHs with total masses higher than $10^8 M_\odot$, LISA will not be able to see the second harmonic at all and so the RWF cannot be used. For both the FWF and the RWF, the errors on the mass and spin parameters are typically worse by a factor of $\sim 1.2 - 4$ when accounting for alternative gravity parameters. The luminosity distance is about $50 - 1000$ times less accurate for the RWF while for the FWF it is only $\sim 10 - 100$ times worse. For the FWF, the sky location error is at maximum 5 times worse while the RWF loses up to a factor of ~ 10 in accuracy.

We present selected distributions of the measurement errors $\Delta m_1/m_1$, $\Delta\chi_1/\chi_1$, $2a$, $\Delta d_L/d_L$ and all the six $\Delta\Psi_i$ in figures 15-24.

C. Correlations between alternative theory parameters

The correlation coefficients for two parameters θ_i and θ_j are given by the normalized covariance matrix as

$$C_{ij} = \frac{\Sigma_{ij}}{\sqrt{\Sigma_{ii}\Sigma_{jj}}}, \tag{66}$$

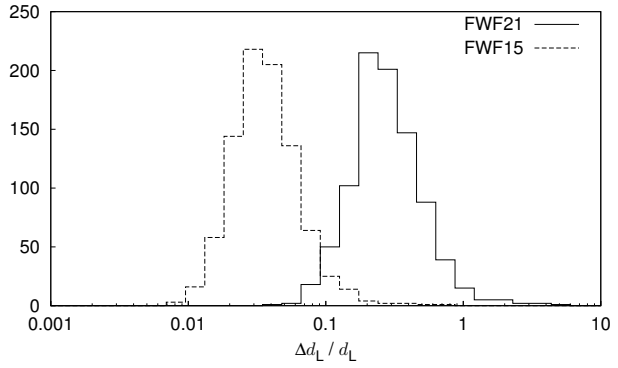

FIG. 18: Comparison between the estimated distributions of the measurement error on d_L for a high-mass binary system $m_1 = 3 \times 10^7 M_\odot$ and $m_2 = 1 \times 10^7 M_\odot$ with (FWF21) and without (FWF15) including alternative theory parameters, using only the restricted waveform.

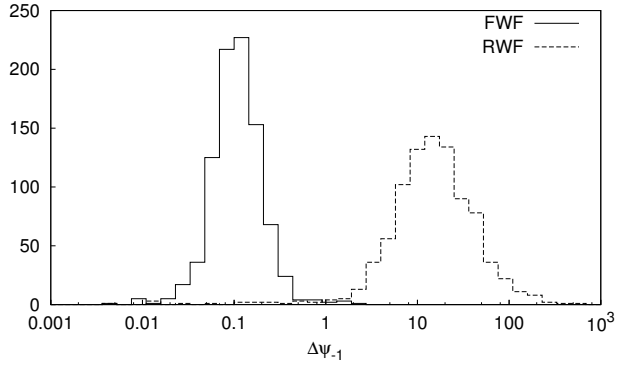

FIG. 19: Comparison between the estimated distributions of the measurement error on the alternative theory parameter Ψ_{-1} for a high-mass binary system $m_1 = 3 \times 10^7 M_\odot$ and $m_2 = 1 \times 10^7 M_\odot$, using the RWF and the FWF.

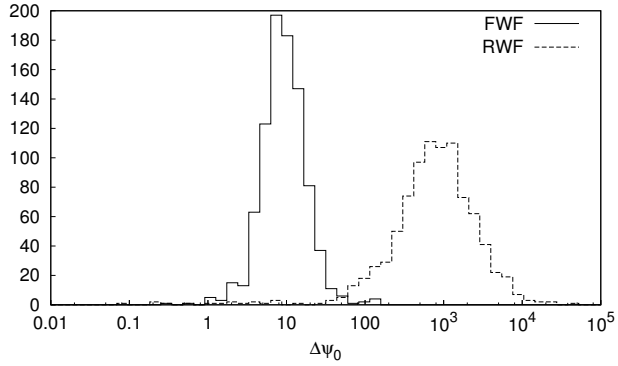

FIG. 20: Comparison between the estimated distributions of the measurement error on the alternative theory parameter Ψ_0 for a high-mass binary system $m_1 = 3 \times 10^7 M_\odot$ and $m_2 = 1 \times 10^7 M_\odot$, using the RWF and the FWF.

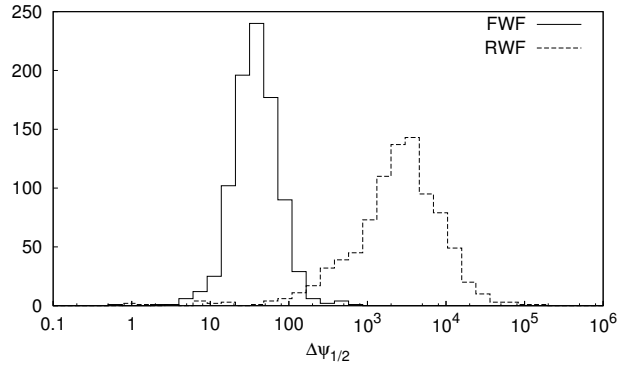

FIG. 21: Comparison between the estimated distributions of the measurement error on the alternative theory parameter $\Psi_{1/2}$ for a high-mass binary system $m_1 = 3 \times 10^7 M_\odot$ and $m_2 = 1 \times 10^7 M_\odot$, using the RWF and the FWF.

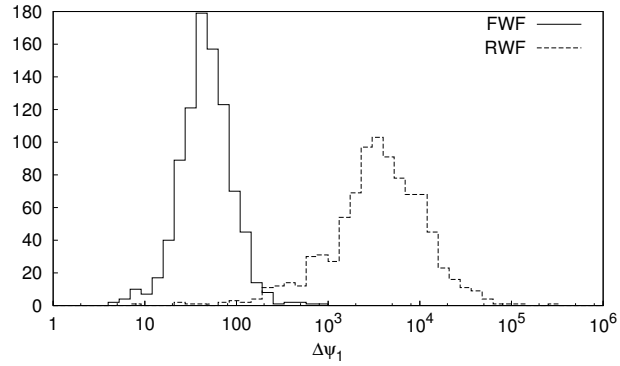

FIG. 22: Comparison between the estimated distributions of the measurement error on the alternative theory parameter Ψ_1 for a high-mass binary system $m_1 = 3 \times 10^7 M_\odot$ and $m_2 = 1 \times 10^7 M_\odot$, using the RWF and the FWF.

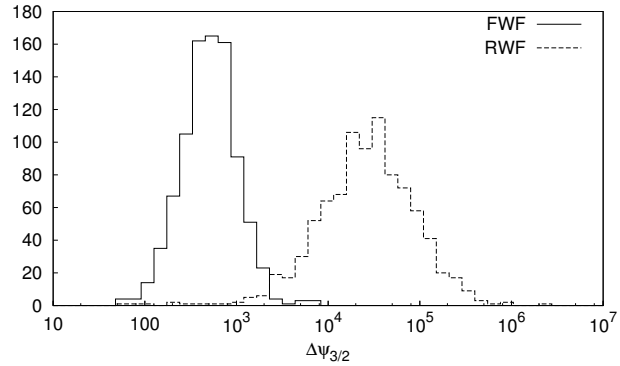

FIG. 23: Comparison between the estimated distributions of the measurement error on the alternative theory parameter $\Psi_{3/2}$ for a high-mass binary system $m_1 = 3 \times 10^7 M_\odot$ and $m_2 = 1 \times 10^7 M_\odot$, using the RWF and the FWF.

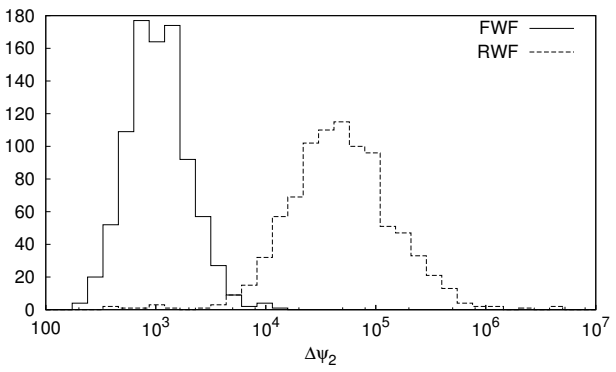

FIG. 24: Comparison between the estimated distributions of the measurement error on the alternative theory parameter Ψ_2 for a high-mass binary system $m_1 = 3\times10^7 M_\odot$ and $m_2 = 1\times10^7 M_\odot$, using the RWF and the FWF.

and are in a range between -1 (perfectly anti-correlated) and 1 (perfectly correlated). Since we are only interested in the mere presence of correlations, we will focus on the absolute value $|C_{ij}|$ varying in the range between 0 (no correlation) and 1.

Because of their simple form in the gravitational wave phase, the alternative theory parameters are expected to correlate highly among each other and with the rest of the phase parameters, especially with the ones which have a similar simple dependency on frequency (and are already highly correlated) like the phase or time at coalescence, ϕ_c and t_c. Often, the use of higher harmonics makes the resulting errors and correlations more complicated and unpredictable: the mostly narrow and symmetric RWF distribution is smeared out over the whole range of possible correlations, usually with a long tail. Also, higher harmonics can in principle introduce new correlations among certain parameters that have not been there before. Below we shortly investigate correlations among the alternative theory parameters and between alternative theory and binary parameters.

1. *Correlations between alternative theory parameters*

We find that the alternative theory parameters can be subdivided into two sets: $\Psi_{\rm low} \equiv \{\Psi_{\text{-}1}, \Psi_0, \Psi_{1/2}\}$ and $\Psi_{\rm high} \equiv \{\Psi_1, \Psi_{3/2}, \Psi_2\}$. The parameters in every set show very high correlations among each other, but less correlation with the parameters of the other set. The parameters in $\Psi_{\rm low}$ have either no fiducial GR phase equivalent with the same frequency power ($\Psi_{\text{-}1}$ and $\Psi_{1/2}$) or one which is fixed to 1 (Ψ_0). In contrast, every parameter in $\Psi_{\rm high}$ can correlate to intrinsic binary parameters with the same frequency dependency, such as masses and spins. Since one integrates over the frequency to compute the Fisher matrix, two parameters have higher correlation if the frequency powers proportional to which they appear in the phase or amplitude are close. So we expect parameters from $\Psi_{\rm high}$ to have higher correlation with the intrinsic binary parameters appearing in the GR phase with the same frequency power than with the $\Psi_{\rm low}$ parameters appearing with lower frequency powers. Consequently, we expect high correlations among the parameters within both sets and also high, but slightly lower correlations between parameters belonging to a different set each. In fig. 25, we plotted the median FWF correlations for selected parameters of both sets against the total mass to illustrate this finding. For two parameters drawn from different sets, the mass ratio also plays an important role for the resulting correlations, while for parameters from the same set, the correlations mainly depend on the total mass.

Within the set $\Psi_{\rm low}$, the FWF is not very effective in breaking the correlations that are present using the RWF model, in some cases it even introduces further correlation. Among theory parameters from the set $\Psi_{\rm high}$, there is a modest correlation breaking for high total masses while for low masses the FWF model stretches out the nearly symmetric RWF correlation distributions by providing them with a long tail on the left-hand side and slightly shifting the peak to the right-hand side (fig. 26). For correlations between two parameters coming out from different sets, there is the same stretching effect and modest correlation breaking for high-masses as for parameters in $\Psi_{\rm high}$, but only for parameters from $\Psi_{\rm low}$ in combination with Ψ_2, a stronger breaking of correlations is achieved by the FWF (fig. 27).

2. *Correlations between binary and theory parameters*

Although there are mass and spin-dependent terms that are proportional to the same frequency power as the alternative theory parameters, mass, spin and angular momentum parameters show only absolute correlations of $\lesssim 0.5$ with the theory parameters, because they enter non-linearly and in several different frequency powers.

The phase and time at coalescence ϕ_c and t_c are formally equivalent to $\Psi_{2.5}$ and Ψ_4, respectively, and are therefore highly correlated with the theory parameters. Especially for tightly correlated parameters, correlations can be broken easily through the introduction of extra structure with higher harmonics. Also the correlations with the sky position parameters μ_n and ϕ_n can be strongly broken for high masses (fig. 28) when using higher harmonics. Interestingly, correlations with the luminosity distance parameter d_L increase for low masses (extra structure can in principle also introduce additional correlations), while there is a modest breaking for high masses (fig. 29).

D. Upper limits for redshifted masses

All the errors tabularized in appendix C are given for the fixed redshift $z = 1$. Some of them in the high-

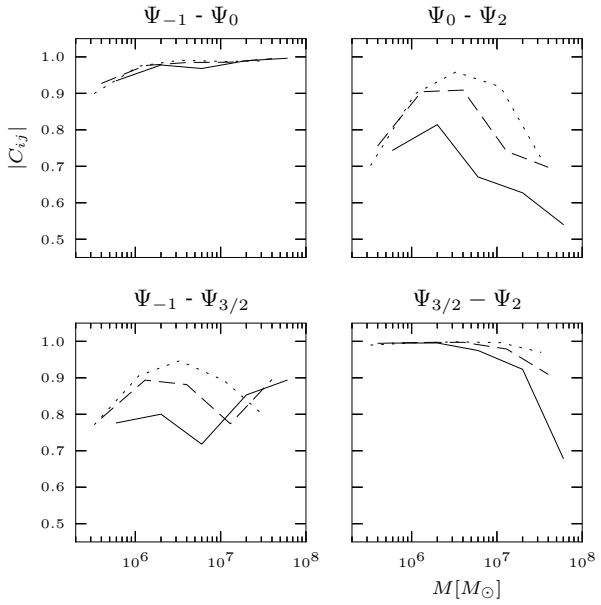

FIG. 25: Median correlations (FWF) between selected alternative theory parameters varying with total mass and shown for each mass ratio independently (1:1 - solid line, 1:3 - dashed line, 1:10 - dotted line). The sets $\{\Psi_{-1}, \Psi_0, \Psi_{1/2}\}$ and $\{\Psi_1, \Psi_{3/2}, \Psi_2\}$ show very high correlations among themselves (top-left, bottom-right) while correlations between theory parameters belonging to different sets are lower (top-right, bottom-left).

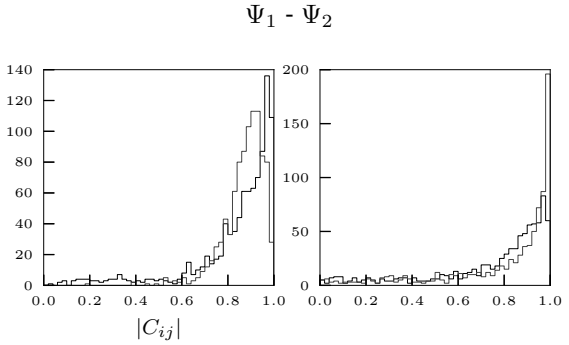

FIG. 26: Correlation breaking for a low-mass $m_1 = 10^6 M_\odot$, $m_2 = 3 \times 10^5 M_\odot$ binary (left) and a $m_1 = 3 \times 10^7 M_\odot$, $m_2 = 10^7 M_\odot$ binary (right). The results of the RWF are indicated with the light-thin line and the results for the FWF with the dark-bold line. For this selected combination of theory parameters, there is modest breaking for high masses.

mass regime are apparently too high at $z = 1$. Nevertheless, since the measurement accuracy of the parameters is correlated with the redshift as given in Eq. (65), for an equivalent mass configuration at a lower redshift the errors should reduce to reasonable values. Since the ac-

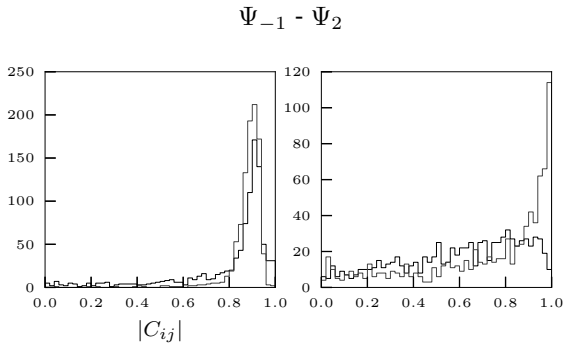

FIG. 27: Correlation breaking for a low-mass $m_1 = 10^6 M_\odot$, $m_2 = 3 \times 10^5 M_\odot$ binary (left) and a $m_1 = 3 \times 10^7 M_\odot$, $m_2 = 10^7 M_\odot$ binary (right). The results of the RWF are indicated with the light-thin line and the results for the FWF with the dark-bold line. For this selected combination of theory parameters, there is stronger correlation breaking for high masses.

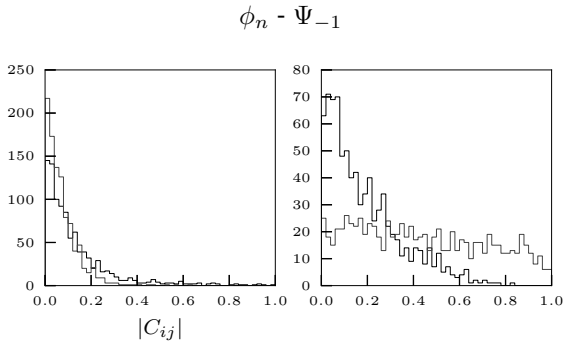

FIG. 28: Correlation breaking for a low-mass $m_1 = 10^6 M_\odot$, $m_2 = 3 \times 10^5 M_\odot$ binary (left) and a $m_1 = 3 \times 10^7 M_\odot$, $m_2 = 10^7 M_\odot$ binary (right). The results of the RWF are indicated with the light-thin line and the results for the FWF with the dark-bold line. When accounting for higher harmonics, correlations of ϕ_n with alternative theory parameters are strongly broken for high masses.

tual values of the alternative theory parameters are not known, we cannot fix the accuracy with which we want to measure $\Psi_i(z)$. For this reason, we introduce the relative accuracy parameter α such that $\Delta\Psi_i(z)/\psi_i < \alpha$ where ψ_i is the fiducial 2PN phase coefficient from $\Psi_{\rm 2PN}$ in Eq. (40). The maximal redshift is then given as

$$z_{\rm max} = z\left(\alpha\, d_L(z_0)\, |\Delta\Psi_i(z_0)/\psi_i|^{-1}\right), \qquad (67)$$

where $z(d_L)$ is the inverse of (14) and can be computed numerically. We use here the 5%-quantile for $\Delta\Psi_i(z_0 = 1)$ as given in the tables in appendix C, i.e. we define the (optimistic) maximal redshift as the redshift where 5% of the binaries in the sample can still be seen with relative accuracy less than α. Since we expect corrections to the 2PN phase parameters of GR to be

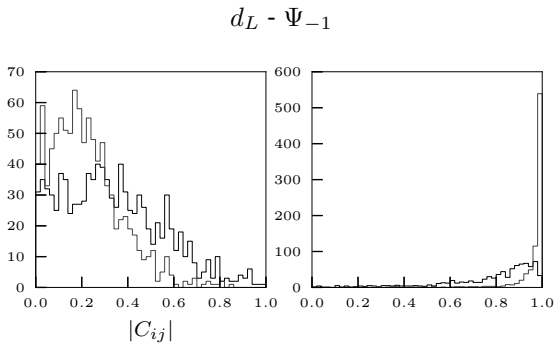

FIG. 29: Correlation breaking for a low-mass $m_1 = 10^6 M_\odot$, $m_2 = 3 \times 10^5 M_\odot$ binary (left) and a $m_1 = 3 \times 10^7 M_\odot$, $m_2 = 10^7 M_\odot$ binary (right). The results of the RWF are indicated with the light-thin line and the results for the FWF with the dark-bold line. For low masses, the correlation with the luminosity distance parameter increases while there is modest breaking for high masses when introducing higher harmonics.

small (at least for the lower PN orders), we focus here on a relative accuracy below 10%. At redshift $z = 1$ this accuracy is already difficult to reach for binaries with masses above $10^6 M_\odot$ (see also [19]). It is important to emphasize that we concentrate here on actually measuring the alternative theory parameters instead of just setting bounds upon them. In figures 30-33 we present the maximal redshifts at which LISA can still measure the alternative theory parameters Ψ_0, Ψ_1, $\Psi_{3/2}$ and Ψ_2 for certain mass configurations with relative accuracies of $\alpha = 10\%$ and $\alpha = 1\%$. Since for Ψ_{-1} and $\Psi_{1/2}$ the fiducial 2PN phase coefficients are zero, we do not consider them. We checked that the error roughly scales with the redshift. For a relative accuracy of 1%, Ψ_0 is measurable up to redshifts of $z \sim 1-10$ for low-mass binaries and up to redshifts of $z \sim 0.01 - 0.1$ for high-mass binaries. Ψ_1, $\Psi_{3/2}$ and Ψ_2 can all be detected with a relative accuracy of 1% up to redshifts of $z \sim 0.1 - 1$ for low masses and $z \sim 0.01 - 0.1$ for high masses. For Ψ_0, the use of the FWF improves the maximal redshifts by about a factor of 2 for low masses and up to a factor of 10 for high masses, while the maximal redshifts are improved by almost an order of magnitude for the rest of the alternative theory parameters. If we were lucky and LISA could find a low-mass black hole binary at very low redshift $z = 0.1$, we would be able to recover the alternative theory parameters with ~ 10 times smaller errors than given in tables XV-XX.

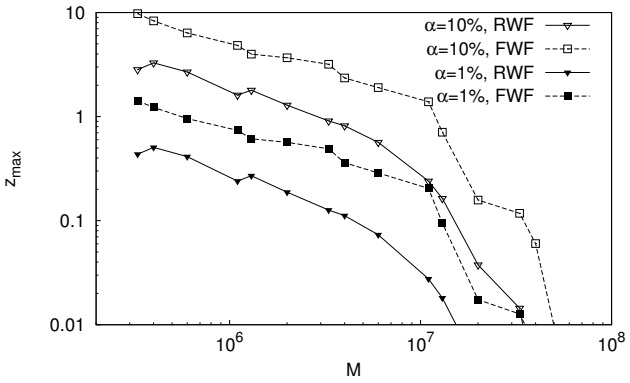

FIG. 31: Maximal redshifts for the alternative theory parameter Ψ_1 such that the relative error $\Delta\Psi_1/\psi_1$ is smaller than α. ψ_1 is the corresponding fiducial 2PN phase coefficient. For a relative error of 1%, low-mass binaries are suitable up to redshifts $z \sim 0.1 - 1$ while high-mass binaries can be observed up to $z \sim 0.01 - 0.1$.

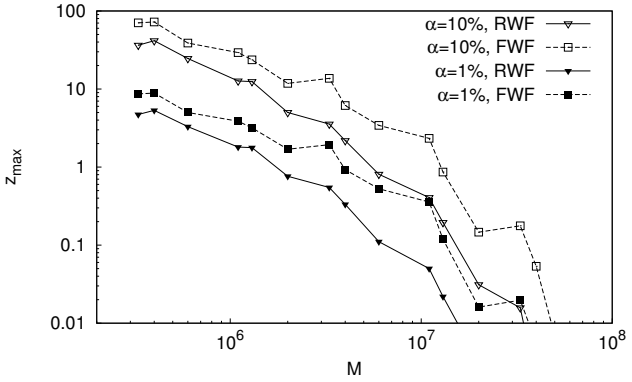

FIG. 30: Maximal redshifts for the alternative theory parameter Ψ_0 such that the relative error $\Delta\Psi_0/\psi_0$ is smaller than α. ψ_0 is the corresponding fiducial 2PN phase coefficient. For a relative error of 1%, low-mass binaries are suitable up to redshifts $z \sim 1 - 10$ while high-mass binaries can be observed up to $z \sim 0.01 - 0.1$.

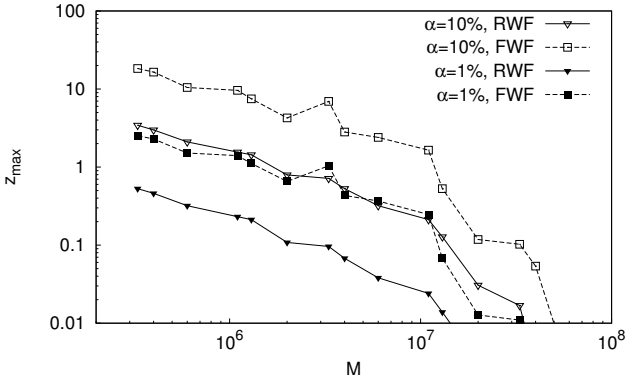

FIG. 32: Maximal redshifts for the alternative theory parameter $\Psi_{3/2}$ such that the relative error $\Delta\Psi_{3/2}/\psi_{3/2}$ is smaller than α. ψ_1 is the corresponding fiducial 2PN phase coefficient. For a relative error of 1%, low-mass binaries are suitable up to redshifts $z \sim 0.1 - 1$ while high-mass binaries can be observed up to $z \sim 0.01 - 0.1$.

E. Example: Lower bound on graviton Compton wavelength

In order to compare our results with previous work in the field, we present here a lower bound on a possible graviton Compton wavelength from our results at redshift $z = 1$. The term 'massive graviton' is commonly used to state that the speed of gravitational waves depends on frequency rather than being constant. According to [6], the effect of a 'massive graviton' can be accounted for by introducing a gravitational wave phase correction

$$\Delta\Psi_{\rm MG}(z) = -\beta(z)\,\nu^{-3/5}\,x^{-3/2}, \tag{68}$$

where x is the dimensionless frequency, ν is the symmetric mass ratio and the parameter $\beta(z)$ is defined as

$$\beta(z) = \frac{G}{c^2}\frac{\pi^2 D(z)\mathcal{M}}{\lambda_g^2(1+z)}. \tag{69}$$

Here λ_g is the Compton wavelength of the graviton, z is the redshift, $\mathcal{M} = (1+z)M\nu^{3/5}$ is the *measured* chirp mass affected by redshift, and $D(z)$ is the distance given as

$$D(z) = (1+z)\frac{c}{H_0}\int_0^z \frac{dz'}{(1+z')^2\sqrt{\Omega_M(1+z')^3+\Omega_\Lambda}}, \tag{70}$$

where H_0, Ω_M and Ω_Λ are defined as in section II. In our implementation, this is similar to the correction in Eq. (40):

$$\Delta\Psi_{\rm MG}(z) = \frac{3}{256\nu}x^{-3/2}\Psi_1(z). \tag{71}$$

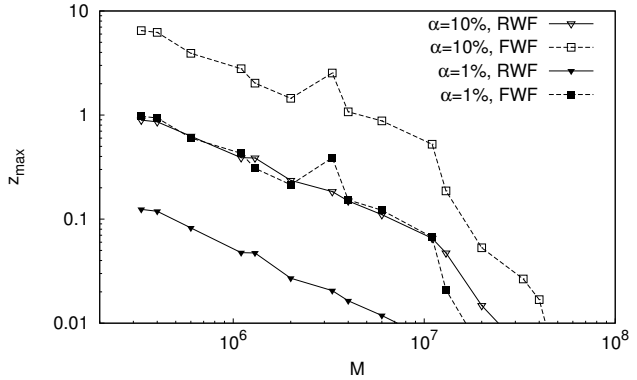

FIG. 33: Maximal redshifts for the alternative theory parameter Ψ_2 such that the relative error $\Delta\Psi_2/\psi_2$ is smaller than α. ψ_2 is the corresponding fiducial 2PN phase coefficient. For a relative error of 1%, low-mass binaries are suitable up to redshifts $z \sim 0.1 - 1$ while high-mass binaries can be observed up to $z \sim 0.01 - 0.1$.

Hence the errors on β and Ψ_1 can be related with

$$\Delta\beta(z) = \frac{3}{256}\nu^{-2/5}\Delta\Psi_1(z). \tag{72}$$

We take the fiducial value $\beta = 0$, thus the error $\Delta\beta$ sets an upper bound on possible values for β. A lower bound on the Compton wavelength of the graviton can then be calculated at redshift z as

$$\lambda_g(z) > \sqrt{\frac{256}{3}\frac{G}{c^2}\frac{\pi^2 D(z) M\nu}{(1+z)\Delta\Psi_1(z)}}, \tag{73}$$

where M is the redshifted total mass of the binary. At redshift $z = 1$ we find that optimal lower bounds on λ_g originate from a $(3\times10^6+1\times10^7)M_\odot$ binary for the FWF and from a $(1\times10^6+1\times10^6)M_\odot$ binary for the RWF. Including all six alternative theory parameters Ψ_i, the resulting average bounds are $\lambda_g > 1.2\times10^{21}$ cm (FWF) and $\lambda_g > 7.8\times10^{20}$ cm (RWF). These bounds are both lower than the one Yagi and Tanaka [15] found ($\lambda_g > 4.9\times10^{21}$ cm) using the RWF and simple precession at a distance of 3 Gpc; this is because the presence of the other five alternative theory parameters increases correlations among the parameters. If we consider only one correction parameter Ψ_1 which among other things accounts for massive gravity, the bounds increase to $\lambda_g > 7.6\times10^{21}$ cm (FWF) and $\lambda_g > 4.9\times10^{21}$ cm (RWF). The RWF bound is slightly higher than the one by Yagi and Tanaka for a $(10^6+10^7)M_\odot$ binary; for this mass configuration we found a lower RWF bound of $\lambda_g > 2.8\times10^{21}$ cm. Cornish et al. [20] found a similar optimal RWF bound of $\lambda_g > 3.8\times10^{21}$ cm. The use of the FWF improves the bound on the graviton Compton wavelength by a factor of ~ 1.6 with respect to the RWF, regardless whether only one or all the alternative theory parameters are included into the simulations. Approximately this factor of accuracy will be lost when going from classic LISA to eLISA/NGO [18].

IX. CONCLUSION AND OUTLOOK

We analyzed the expected measurement error distributions of 17 different mass configurations of supermassive black hole binaries with masses between $10^5 - 10^8 M_\odot$. We found that the black hole binaries can roughly be divided into two groups: low-mass binaries with $M \lesssim 10^7 M_\odot$ and high-mass binaries with $M \gtrsim 10^7 M_\odot$. Comparing the results of the simulations using the FWF and the RWF, we found that the RWF errors on the alternative theory parameters Ψ_i are a factor of ~ 100 times higher than the FWF errors for high-mass binaries, while they are almost comparable for low-mass binaries. Due to the dilution of the available information through the introduction of six extra parameters, the original parameters lose accuracy. For masses and spins this is only a

factor of 1.2-5 for both low- and high-mass binaries regardless of whether the FWF or RWF is used. The loss of accuracy on the position of the black hole binary on the sky is at maximum 10% for low-mass binaries and up to a factor of 5 for high-mass binaries. However, the accuracy of the luminosity distance is affected more seriously for high-mass binaries, using the RWF results in a loss of a factor of $\sim 50-1000$ while using the FWF reduces it to factors of $\sim 10-100$. For low-mass binaries it is only about a factor of 2 worse. The use of the FWF is therefore mandatory for high-mass binaries, while the parameter estimation is more efficient for low-mass binaries and only up to a factor of 5 times worse when the RWF is used instead of the FWF.

Since the error distributions were all calculated at fixed redshift $z = 1$ but the errors increase with redshift, we computed typical maximal redshifts up to which the alternative theory parameters are detectable with a relative accuracy smaller than 1% for the best 5% of the binaries in the sample. We found that for a deviation of 1% from the fiducial value, Ψ_0 is detectable up to redshifts of $z \sim 1-10$ for low total masses and up to $z \sim 0.01-0.1$ for high total masses. The rest of the alternative theory parameters Ψ_1, $\Psi_{3/2}$ and Ψ_2 with a fiducial 2PN phase coefficient unequal zero are detectable up to redshifts of $z \sim 0.1-1$ for low-mass binaries and $z \sim 0.01-0.1$ for high-mass binaries with the same relative accuracy. The use of the FWF improves the maximal redshifts up to a factor of 10 for high total masses.

The FWF enables us to increase the optimal lower bound on the Compton wavelength of the graviton by about a factor of 1.6 compared to the one reached by the RWF. We achieve an optimal lower bound of $\lambda_g > 7.6 \times 10^{21}$ cm for the classic LISA detector design if only the alternative theory parameter Ψ_1 is considered.

Since the proposed eLISA/NGO mission will most certainly fly as a reduced variant of classic LISA, it is important to investigate the reassessment of certain aspects of the mission. A broad range of LISA variants are currently reviewed by the community. To account for the technical 'shortcomings' it is thus of great importance to use as accurate waveform templates as possible to restore the lost accuracy with computational power on Earth. The use of the FWF improves the accuracy of the alternative theory parameters by at least an order of magnitude compared to the RWF. As shown by [16], the use of hybrid inspiral-merger-ringdown templates instead of inspiral-only templates improves the accuracy by an order of magnitude for the RWF; it would be interesting to find out how much such templates are improved when the FWF is used. The accuracy can further be enhanced by about an order of magnitude when considering combined observations instead of just extracting alternative theory parameters from individual black hole binaries [18]. Also effects of eccentric orbits should be accounted for to make the model more realistic.

Future work could include the introduction of amplitude corrections such as in [8], since certain alternative theories have dominant contributions in the gravitational wave amplitude (e.g. Chern-Simons-modified gravity [44]). Also, the underlying mechanism of spin precession should be analyzed for effects originating from possible alternative theories. In this paper we neglected the energy loss of black hole binaries through unexpected physical effects such as further degrees of freedom in the propagation of gravitational waves arising from additional polarizations (e.g. longitudinal modes). It would be interesting to introduce a parametrized model for these effects [45] into our simulations. Also, since we studied a search for modifications at different PN orders at the same time, one could use the results of this work to investigate how the use of next-to-leading order modifications of GR could affect the determination of alternative theory parameters. The impact of turning off and on correction parameters also needs further studies (following e.g. [36]).

Acknowledgments

C. H. would like to thank Sylvain Marsat for interesting discussions about the post-Newtonian expansion and Ed Porter for his suggestions for improvements on our code. The authors appreciate the valuable comments by the anonymous referee. C. H. and A. K. are supported by the Swiss National Science Foundation.

Appendix A: Breakdown conditions

Since in previous work different viewpoints are taken on the choice of a critical orbit at which the integrations need to be stopped for binary black holes with precessing spins, we give here a quick summary of the approximations we used for the gravitational wave signal generation and indicate at which point we consider them to have failed. The three major assumptions are that orbits can be considered to be quasi-circular (adiabatic approximation), the spins can be treated as constants over one orbit (orbit-averaged spin precession) and the weak field or post-Newtonian approximation, which assumes typical velocities to be smaller than the speed of light, which enables us to perform a PN expansion in terms of powers of v/c. We shall discuss below how to estimate at which point the breakdown of these assumptions occurs; in particular, the breakdown of the PN approximation can be estimated using different methods, among which the use of the minimum energy circular orbit (MECO) or the PN energy flux is common.

We decided to stop our integrations always at the ISCO of $6\,GM/c^2$, since orbit-averaged spin precession can already start to be inaccurate at this point and the authors do not trust the PN expansion below this limit. Also we did not find any binary system with a minimum energy circular orbit, flux or adiabatic breakdown higher than this radius. In the following subsection we list four dif-

ferent approximations criteria and discuss the limits of their validity.

1. Adiabatic approximation

The adiabatic approximation assumes that the time needed for one orbit is much smaller than the timescale for orbit shrinkage. In other words, the orbit shrinkage velocity $\dot{r} = \frac{dr}{dt}$ is required to be much smaller than the orbital velocity ωr, then the orbits can be considered to be quasi-circular. The orbital separation is given (expanded in terms of the dimensionless frequency x up to 2PN order) by

$$r(x) = \frac{GM}{c^2 x}\left[1 + \frac{1}{3}(-3+\nu)x - \frac{1}{3}\beta(2,3)x^{3/2} + \left(\frac{19}{4}\nu + \frac{1}{9}\nu^2 - \frac{1}{2}\sigma(1,3)\right)x^2\right], \tag{A1}$$

where β and σ (expected to vary only slowly on one orbit) have been treated as constants. As an indicator for the faithfulness of the adiabatic approximation, we choose the expression

$$\frac{|\dot{r}|}{\omega r} < \kappa_{\rm adiab}. \tag{A2}$$

The quantities ωr and $\dot{r} = \frac{dr}{dx}\frac{dx}{dt}$ can be computed to stop the integration when a certain adiabatic breakdown limit $\kappa_{\rm adiab}$ of our choice is reached. The breakdown radius for constant $\kappa_{\rm adiab}$ shows almost linear dependency on the initial value of $\hat{\boldsymbol{L}} \cdot \boldsymbol{S}_{\rm eff}$ (when the binary enters the LISA band). In figs. 34 and 35, the adiabatic breakdown limits for $\kappa_{\rm adiab} = 0.1, 0.3$ and 1.0 are plotted for 10^3 randomly distributed systems in the parameter space with equal masses and a mass ratio of 1:10 respectively. The figures indicate that the adiabatic approximation is still quite reasonable ($\kappa_{\rm adiab} < 0.1$) for orbital separations larger than $r = 5\,GM/c^2$, so we do not have to consider it since we already stop before this limit.

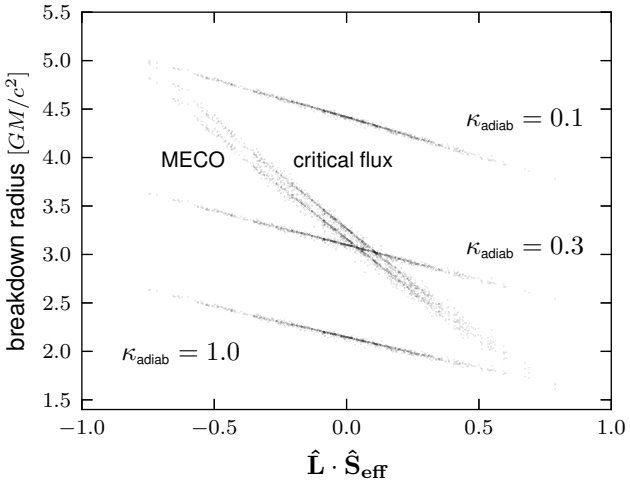

FIG. 34: Plot of MECO radius, critical flux radius and adiabatic breakdown radii (for different limits $\kappa_{\rm adiab}$) against the initial effective spin orientation for 1000 simulated systems with two equal mass $2 \times 10^6 M_\odot$ black holes (binary of two $10^6 M_\odot$ black holes seen at redshift $z = 1$).

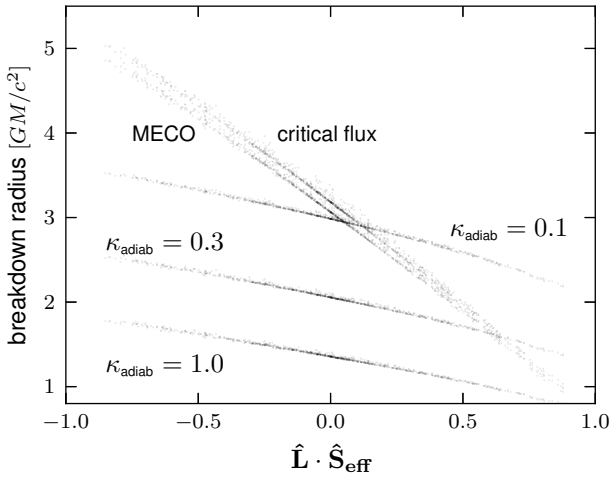

FIG. 35: Plot of MECO radius, critical flux radius and adiabatic breakdown radii (for different limits $\kappa_{\rm adiab}$) against the initial effective spin orientation for 1000 simulated systems with black hole binaries of mass ratio 1:10 ($m_1 = 2 \times 10^7 M_\odot$, $m_2 = 2 \times 10^6 M_\odot$).

2. MECO

The last stable circular orbit (ISCO) for test masses orbiting a non-spinning, Schwarzschild black hole takes place at the minimum of the effective gravitational potential $\frac{dV_{\rm eff}}{dr} = 0$, corresponding to an orbital separation of 6 GM/c^2. This is of course different for black hole binaries with comparable masses and non-zero spins; there, the total energy is only known in terms of a PN expansion [46–48]

$$E = -\frac{\mu c^2}{2} x\left(1 - \frac{1}{12}(9+\nu)x + \frac{c}{G}\frac{4}{3M^2}\hat{\boldsymbol{L}} \cdot \boldsymbol{S}_{\rm eff}\, x^{3/2} + \left[\frac{1}{24}(-81 + 57\nu - \nu^2) + \frac{c^2}{G^2}\frac{1}{\nu M^4}(\boldsymbol{S}_1 \cdot \boldsymbol{S}_2 - 3(\hat{\boldsymbol{L}} \cdot \boldsymbol{S}_1)(\hat{\boldsymbol{L}} \cdot \boldsymbol{S}_2))\right] x^2\right), \tag{A3}$$

including leading order spin-spin and spin-orbit couplings. The effective spin $\boldsymbol{S}_{\rm eff}$ is defined as the combination

$$\boldsymbol{S}_{\rm eff} = \left(2+\frac{3m_2}{2m_1}\right)\boldsymbol{S}_1 + \left(2+\frac{3m_1}{2m_2}\right)\boldsymbol{S}_2. \qquad \text{(A4)}$$

The last stable circular orbit is then thought to take place at the point where

$$\frac{dE}{dx} = 0,$$

the *minimum energy circular orbit* (MECO). Afterwards the binaries are thought to plunge and quasi-circular orbit approximations will certainly fail. In figures 34 and 35, the MECO radii for 10^3 randomly distributed systems in the parameter space are plotted for mass ratios of 1:1 and 1:10 respectively. The MECO radius is always below the radius where the gravitational wave energy flux reaches a critical limit (defined in the next subsection), so we do not consider the MECO as a breakdown criterion for our simulations but instead use the flux condition worked out in the next subsection.

3. Flux

The energy flux of a gravitational wave can be expressed as [21]

$$\begin{aligned}\mathcal{L} &= -\frac{dE}{dt} = -\frac{dx}{dt}\frac{dE}{dx} \\ &= \frac{32c^5}{5G}\nu^2 x^5\left[1-\left(\frac{1247}{336}+\frac{35}{12}\nu\right)x+\alpha_{3/2}x^{3/2}+\alpha_2 x^2\right],\end{aligned} \qquad \text{(A5)}$$

where $\frac{dx}{dt}$ and E are the 2PN expressions used in this paper. For the expressions $\alpha_{3/2}$ and α_2 containing spin-orbit and spin-spin couplings, the reader is referred to [21]. As long as x is small, this flux will stay close to its leading order contribution. As soon as x gets close to 1, the 1PN term will grow stronger, decrease the flux and eventually make it negative [49]. One can thus infer that the PN series tends to breakdown if $\mathcal{L}$ deviates significantly from its leading order contribution and has for sure broken down if the flux is negative.

We decided to stop the integrations if the flux is smaller than 10% of its leading order contribution (with spin-angular momentum and spin-spin terms included). The plots in figures 34 and 35 show that the critical flux is never reached above $r = 5\,GM/c^2$, which means that there are no black hole binaries with a MECO higher than $r = 6\,GM/c^2$ in our mass range which could potentially lead to unphysical results. Nevertheless, we use a catch in our code to stop the integration if the flux gets by an unforeseen chance smaller than 10% of its leading order contribution. Especially for parallel spins, one could theoretically try to go even down to $2-4\,GM/c^2$. In these regions a lot more SNR could be accumulated, resulting in a ~ 10 times higher overall SNR and sometimes several orders of magnitude smaller errors. This is very dangerous, since we do not expect post-Newtonian theory to be physically accurate enough in these regions and one should be suspicious of such small errors.

4. Orbit-averaged spin precession

Since we use orbit-averaged spin precession equations [23], we need to assure that the underlying assumption of the timescale for precession always being smaller than the orbital time still holds. Like other recent studies (see e.g. [43]), we do not consider the breakdown of this approximation in our integrations, since both timescales are comparable only around $2-3\;GM/c^2$. We are however not sure, how strongly errors in the spin precession affect the matched filtering process. Since large spin precession occurs only in the late inspiral (where the largest part of the SNR is accumulated), an improper treatment of orbit-averaged spin precession creates a theoretical error in the waveform template and thus could result in a significant loss of SNR, despite the fact that the Fisher matrix gave an optimistic error estimate. We plan to quantify this theoretical error in a future publication.

In this subsection, we present the breakdown radii corresponding to certain limits on the angular momentum precession timescale, i.e. the critical orbits where the integration should be stopped.

The timescale for one full orbit is

$$T_{\rm orb} = 2\pi\sqrt{\frac{r^3}{GM}}. \qquad \text{(A6)}$$

Ignoring spin-spin terms, the precession of the angular momentum unit vector can then be written as (see e.g. [50])

$$\dot{\hat{\boldsymbol{L}}} = \frac{G}{c^2 r^3}\boldsymbol{S}_{\rm eff}\times\hat{\boldsymbol{L}}, \qquad \text{(A7)}$$

with the effective spin vector $\boldsymbol{S}_{\rm eff}$ defined in (A4). Thus $\hat{\boldsymbol{L}}$ precesses with an angular frequency of approximately $\omega_{\rm prec} = \frac{G}{c^2 r^3}|\boldsymbol{S}_{\rm eff}|$ which corresponds to a time of

$$T_{\rm prec} = 2\pi\frac{c^2 r^3}{G|\boldsymbol{S}_{\rm eff}|} \qquad \text{(A8)}$$

for one precession. A good indicator for the breakdown of orbit-averaged spin precession is thus the fraction

$$\frac{T_{\rm orb}}{T_{\rm prec}} < \kappa_{\rm prec}, \qquad \text{(A9)}$$

where $\kappa_{\rm prec}$ is the critical limit of our choice. In the case where the two timescales are equal ($\kappa_{\rm prec} = 1$), this corresponds to a full precession in one orbit. At this point one certainly cannot speak of 'orbit-averaged' spin precession anymore.

The maximum absolute value which the effective spin is able to reach can be found to be $|\boldsymbol{S}_{\rm eff}| = \frac{GM^2}{c}(2-\nu)$, for two aligned, maximally spinning black holes. Hence we can write the effective spin introducing a dimensionless strength $0 \leq \chi_{\rm eff} < 1$ as

$$|\boldsymbol{S}_{\rm eff}| = \chi_{\rm eff}\frac{GM^2}{c}(2-\nu). \tag{A10}$$

From eqs. (A6) - (A9) we can then infer the critical radius where the orbit-averaged precession equations break down (slightly perturbed by fluctuations coming from neglected spin-spin terms):

$$r = \left(\frac{(2-\nu)\chi_{\rm eff}}{\kappa_{\rm prec}}\right)^{2/3}\frac{GM}{c^2}. \tag{A11}$$

In figures 36 and 37, numerical simulations (including spin-spin terms) are shown, where 10^3 binary systems with mass ratios 1:1 and 1:10 (and uniformly distributed parameters) are used, respectively. The simulations match with the predictions by eq. (A11). For high effective spins, the integrations should be stopped already around $r = 6\,GM/c^2$ in the conservative limit ($\kappa_{\rm prec} = 0.1$) and $r = 2\,GM/c^2$ in a very optimistic limit ($\kappa_{\rm prec} = 1$). Since we stop at $r = 6\,GM/c^2$, we chose to ignore the breakdown of orbit-averaged spin precession in the current work, but emphasize that theoretical errors arising from this assumption should be investigated in the future.

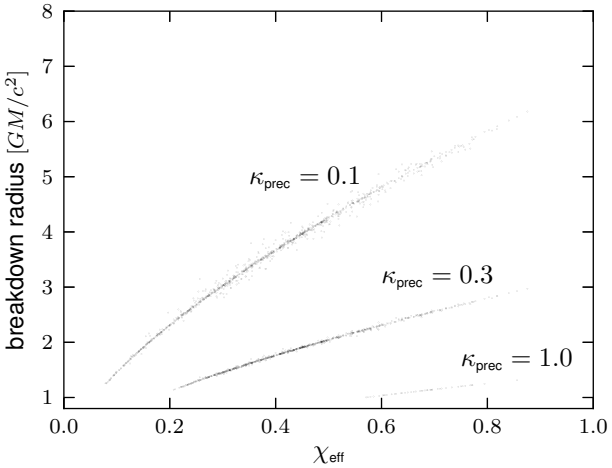

FIG. 36: Plot of orbit-averaged precession breakdown radii (for different limits $\kappa_{\rm prec}$) against the initial effective spin strength for 1000 simulated systems with two equal mass $2 \times 10^6 M_\odot$ black holes.

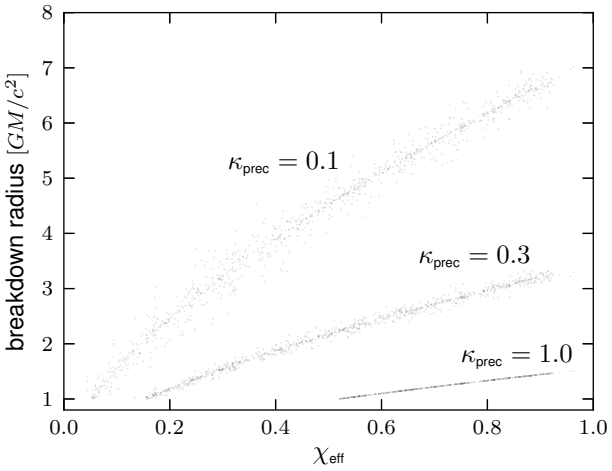

FIG. 37: Plot of orbit-averaged precession breakdown radii (for different limits $\kappa_{\rm prec}$) against the initial effective spin strength for 1000 simulated systems with black hole binaries of mass ratio 1:10 ($m_1 = 2 \times 10^7 M_\odot$, $m_2 = 2 \times 10^6 M_\odot$).

Appendix B: The 2.5PN and 3PN orbital frequency evolution equations

The inclusion of dipole radiation corrections proportional to x^{-1} requires the knowledge of higher PN orders to be consistent to 2PN order, namely 2.5PN and 3PN contributions. Since the current 2.5PN expansion just considers spin-orbit contributions and no spin-spin effects, and the 3PN expansion does not account for any spin coupling effects at all, these are of course only approximations.

1. 2.5PN from Blanchet et al. 2006

Blanchet et al. 2006 [22] compute the angular frequency evolution for a binary with symmetric mass ratio ν as

$$\frac{\dot{\omega}}{\omega^2} = \frac{96}{5}\nu x^{5/2}\left\{1+x\left(-\frac{743}{336}-\frac{11}{4}\nu\right)+4\pi x^{3/2} +x^2\left(\frac{34103}{18144}+\frac{13661}{2016}\nu+\frac{59}{18}\nu^2\right)+ \pi x^{5/2}\left(-\frac{4159}{672}-\frac{189}{8}\nu\right)+\frac{x^{3/2}}{Gm^2}\left[-\frac{47}{3}S_l -\frac{25}{4}\frac{\delta m}{m}\Sigma_l\right]+\frac{x^{5/2}}{Gm^2}\left[\left(-\frac{40127}{1008}+\frac{1465}{28}\nu\right)S_l + \left(-\frac{583}{42}+\frac{3049}{168}\nu\right)\frac{\delta m}{m}\Sigma_l\right]+O\left(\frac{1}{c^6}\right)\ , \tag{B1}$$

where $\omega = c^3/(GM)\ x^{3/2}$, $\delta m = m_1 - m_2$ is the mass difference and $m = m_1 + m_2$ is the total mass. The spin interaction terms are expressed with

$$\boldsymbol{\Sigma} = m\left[\frac{\boldsymbol{S}_2}{m_2}-\frac{\boldsymbol{S}_1}{m_1}\right], \qquad S_l = \boldsymbol{S}\cdot\boldsymbol{l}, \qquad \Sigma_l = \boldsymbol{\Sigma}\cdot\boldsymbol{l}, \tag{B2}$$

where $\boldsymbol{S} = \boldsymbol{S}_1 + \boldsymbol{S}_2$ is the total spin and $\boldsymbol{l} = \frac{\boldsymbol{L}}{|\boldsymbol{L}|}$ is the angular momentum unit vector. This enables us to write Eq. (B1) in the same form as Eq. (18), and we recover

$$b_{5/2} = \pi\left(-\frac{4159}{672}-\frac{189}{8}\nu\right)+\frac{1}{Gm^2}\left[\left(-\frac{40127}{1008} + \frac{1465}{28}\nu\right)S_l+\left(-\frac{583}{42}+\frac{3049}{168}\nu\right)\frac{\delta m}{m}\Sigma_l\right]. \tag{B3}$$

2. 3PN without spin terms from Blanchet et al. 2002

In Luc Blanchet's living review [21] (see also [51–53]), the 3PN expression for the total energy of non-spinning compact binaries can be found to be

$$E = -\frac{1}{2}\mu c^2 x\left\{1+\left(-\frac{3}{4}-\frac{1}{12}\nu\right)x+\left(-\frac{27}{8}+\frac{19}{8}\nu -\frac{1}{24}\nu^2\right)x^2+\left(-\frac{675}{64}+\left[\frac{34445}{576}-\frac{205}{96}\pi^2\right]\nu -\frac{155}{96}\nu^2-\frac{35}{5184}\nu^3\right)x^3\right\}\ , \tag{B4}$$

and the energy flux is

$$\frac{dE}{dt} = -\frac{32c^5}{5G}\nu^2 x^5\left\{1+\left(-\frac{1247}{336}-\frac{35}{12}\nu\right)x+4\pi x^{3/2} +\left(-\frac{44711}{9072}+\frac{9271}{504}\nu+\frac{65}{18}\nu^2\right)x^2+\left(-\frac{8191}{672} -\frac{535}{24}\nu\right)\pi x^{5/2}+\left(\frac{6643739519}{69854400}+\frac{16}{3}\pi^2-\frac{1712}{105}C -\frac{856}{105}\log(16x)+\left[-\frac{134543}{7776}+\frac{41}{48}\pi^2\right]\nu-\frac{94403}{3024}\nu^2 -\frac{775}{324}\nu^3\right)x^3+\left(-\frac{16285}{504}+\frac{176419}{1512}\nu+\frac{19897}{378}\nu^2\right) \times\pi x^{7/2}\right\}. \tag{B5}$$

Here ν is the symmetric mass ratio and $C = 0.577..$ is the Euler constant. The logarithm in dE/dt will lead to a logarithmic term in the 3PN expansion. The PN coefficients b_i can be recovered by computing the frequency evolution as a series in the dimensionless frequency x in the adiabatic approximation:

$$\frac{dx}{dt} = \frac{dE}{dt}\left(\frac{dE}{dx}\right)^{-1} = \frac{64\nu}{5}\frac{c^3}{Gm}x^5\left[b_1 x + b_{3/2}x^{3/2}+b_2x^2+b^{5/2}x^{5/2} +b_3x^3+b_{3,\log}x^3\log(x)\right], \tag{B6}$$

with

$$b_3 = \frac{16447322263}{139708800}-\frac{1712\gamma_e}{105}+\frac{16\pi^2}{3}-\frac{56198689\nu}{217728} +\frac{451\pi^2\nu}{48}+\frac{541\nu^2}{896}-\frac{5605\nu^3}{2592}-\frac{856}{105}\log(16),$$
$$b_{3,\log} = -\frac{856}{105}. \tag{B7}$$

Appendix C: Tables

TABLE I: Median, 5% and 95% quantiles of the estimated measurement errors on m_1 for different mass configurations at redshift $z = 1$ with alternative theory parameters included.

$m_1[M_\odot]$	$m_2[M_\odot]$	$\Delta m_1/m_1$ with corrections					
		5%-quantile		Median		95%-quantile	
		RWF	FWF	RWF	FWF	RWF	FWF
3×10^5	3×10^4	5.2×10^{-4}	4.0×10^{-4}	1.4×10^{-3}	1.1×10^{-3}	7.1×10^{-3}	2.7×10^{-3}
3×10^5	1×10^5	5.1×10^{-4}	4.0×10^{-4}	1.6×10^{-3}	8.8×10^{-4}	1.1×10^{-2}	2.3×10^{-3}
3×10^5	3×10^5	6.4×10^{-4}	4.1×10^{-4}	2.4×10^{-3}	1.0×10^{-3}	1.5×10^{-2}	2.7×10^{-3}
1×10^6	1×10^5	1.2×10^{-3}	7.9×10^{-4}	2.8×10^{-3}	1.8×10^{-3}	1.4×10^{-2}	4.4×10^{-3}
1×10^6	3×10^5	1.1×10^{-3}	7.5×10^{-4}	3.3×10^{-3}	1.7×10^{-3}	1.9×10^{-2}	4.0×10^{-3}
1×10^6	1×10^6	1.3×10^{-3}	8.9×10^{-4}	6.2×10^{-3}	2.7×10^{-3}	6.6×10^{-2}	6.6×10^{-3}
3×10^6	3×10^5	2.3×10^{-3}	1.4×10^{-3}	6.0×10^{-3}	2.8×10^{-3}	3.3×10^{-2}	6.5×10^{-3}
3×10^6	1×10^6	2.5×10^{-3}	1.2×10^{-3}	1.1×10^{-2}	2.9×10^{-3}	6.6×10^{-2}	7.8×10^{-3}
3×10^6	3×10^6	4.9×10^{-3}	2.1×10^{-3}	3.2×10^{-2}	9.0×10^{-3}	0.33	2.7×10^{-2}
1×10^7	1×10^6	1.1×10^{-2}	2.1×10^{-3}	3.7×10^{-2}	4.0×10^{-3}	0.12	9.6×10^{-3}
1×10^7	3×10^6	2.1×10^{-2}	1.9×10^{-3}	9.0×10^{-2}	4.9×10^{-3}	0.34	1.5×10^{-2}
1×10^7	1×10^7	0.17	1.6×10^{-2}	0.83	3.4×10^{-2}	4.2	7.5×10^{-2}
3×10^7	3×10^6	0.14	5.6×10^{-3}	0.37	1.1×10^{-2}	1.1	2.2×10^{-2}
3×10^7	1×10^7	0.42	9.2×10^{-3}	1.1	2.0×10^{-2}	3.6	5.0×10^{-2}
3×10^7	3×10^7	3.7	5.8×10^{-2}	29	0.15	250	0.5
1×10^8	1×10^7	∞	0.13	∞	0.36	∞	1.5
1×10^8	3×10^7	∞	1.3	∞	3.8	∞	40

TABLE II: Median, 5% and 95% quantiles of the estimated measurement errors on m_1 for different mass configurations at redshift $z = 1$ without considering alternative theory parameters.

$m_1[M_\odot]$	$m_2[M_\odot]$	$\Delta m_1/m_1$ without corrections					
		5%-quantile		Median		95%-quantile	
		RWF	FWF	RWF	FWF	RWF	FWF
3×10^5	3×10^4	1.1×10^{-4}	8.2×10^{-5}	3.2×10^{-4}	2.4×10^{-4}	2.5×10^{-3}	2.5×10^{-3}
3×10^5	1×10^5	1.8×10^{-4}	1.4×10^{-4}	7.7×10^{-4}	4.5×10^{-4}	8.2×10^{-3}	8.2×10^{-3}
3×10^5	3×10^5	2.1×10^{-4}	1.4×10^{-4}	1.2×10^{-3}	2.9×10^{-4}	9.1×10^{-3}	9.1×10^{-3}
1×10^6	1×10^5	2.2×10^{-4}	1.5×10^{-4}	7.0×10^{-4}	4.2×10^{-4}	5.1×10^{-3}	5.1×10^{-3}
1×10^6	3×10^5	3.9×10^{-4}	2.7×10^{-4}	1.4×10^{-3}	8.6×10^{-4}	1.3×10^{-2}	1.3×10^{-2}
1×10^6	1×10^6	3.6×10^{-4}	2.6×10^{-4}	2.5×10^{-3}	6.9×10^{-4}	3.2×10^{-2}	3.2×10^{-2}
3×10^6	3×10^5	4.1×10^{-4}	2.3×10^{-4}	1.2×10^{-3}	6.6×10^{-4}	1.4×10^{-2}	1.4×10^{-2}
3×10^6	1×10^6	9.1×10^{-4}	5.0×10^{-4}	3.9×10^{-3}	1.2×10^{-3}	4.0×10^{-2}	4.0×10^{-2}
3×10^6	3×10^6	1.0×10^{-3}	3.8×10^{-4}	8.5×10^{-3}	8.3×10^{-4}	0.11	0.11
1×10^7	1×10^6	1.1×10^{-3}	4.0×10^{-4}	4.1×10^{-3}	1.3×10^{-3}	4.8×10^{-2}	4.8×10^{-2}
1×10^7	3×10^6	3.4×10^{-3}	7.9×10^{-4}	1.6×10^{-2}	1.8×10^{-3}	0.16	0.16
1×10^7	1×10^7	2.4×10^{-2}	2.1×10^{-3}	0.2	5.5×10^{-3}	1.6	1.6
3×10^7	3×10^6	1.4×10^{-2}	1.6×10^{-3}	9.0×10^{-2}	5.0×10^{-3}	0.55	0.55
3×10^7	1×10^7	0.38	4.4×10^{-3}	0.97	9.8×10^{-3}	3.1	3.1
3×10^7	3×10^7	3.2	5.1×10^{-2}	22	0.13	120	120
1×10^8	1×10^7	∞	0.1	∞	0.26	∞	∞
1×10^8	3×10^7	∞	0.92	∞	2.8	∞	∞

TABLE III: Median, 5% and 95% quantiles of the estimated measurement errors on m_2 for different mass configurations at redshift $z = 1$ with alternative theory parameters included.

$m_1[M_\odot]$	$m_2[M_\odot]$	$\Delta m_2/m_2$ with corrections					
		5%-quantile		Median		95%-quantile	
		RWF	FWF	RWF	FWF	RWF	FWF
3×10^5	3×10^4	1.6×10^{-4}	1.2×10^{-4}	5.6×10^{-4}	4.0×10^{-4}	4.8×10^{-3}	2.2×10^{-3}
3×10^5	1×10^5	3.2×10^{-4}	2.2×10^{-4}	1.1×10^{-3}	7.6×10^{-4}	9.2×10^{-3}	2.3×10^{-3}
3×10^5	3×10^5	6.4×10^{-4}	4.2×10^{-4}	2.4×10^{-3}	1.0×10^{-3}	1.6×10^{-2}	2.6×10^{-3}
1×10^6	1×10^5	3.4×10^{-4}	2.3×10^{-4}	1.3×10^{-3}	8.7×10^{-4}	1.3×10^{-2}	4.5×10^{-3}
1×10^6	3×10^5	7.1×10^{-4}	4.9×10^{-4}	2.3×10^{-3}	1.5×10^{-3}	1.7×10^{-2}	4.1×10^{-3}
1×10^6	1×10^6	1.2×10^{-3}	8.8×10^{-4}	6.4×10^{-3}	2.7×10^{-3}	6.5×10^{-2}	6.6×10^{-3}
3×10^6	3×10^5	7.5×10^{-4}	4.8×10^{-4}	2.6×10^{-3}	1.5×10^{-3}	3.2×10^{-2}	7.8×10^{-3}
3×10^6	1×10^6	1.7×10^{-3}	8.4×10^{-4}	6.6×10^{-3}	3.0×10^{-3}	5.5×10^{-2}	1.0×10^{-2}
3×10^6	3×10^6	4.5×10^{-3}	2.1×10^{-3}	3.2×10^{-2}	9.0×10^{-3}	0.33	2.7×10^{-2}
1×10^7	1×10^6	3.0×10^{-3}	1.1×10^{-3}	1.2×10^{-2}	3.8×10^{-3}	9.6×10^{-2}	1.8×10^{-2}
1×10^7	3×10^6	6.1×10^{-3}	1.7×10^{-3}	2.9×10^{-2}	6.6×10^{-3}	0.27	2.6×10^{-2}
1×10^7	1×10^7	0.17	1.6×10^{-2}	0.8	3.4×10^{-2}	4.2	7.5×10^{-2}
3×10^7	3×10^6	7.5×10^{-2}	5.5×10^{-3}	0.38	1.8×10^{-2}	2.3	6.4×10^{-2}
3×10^7	1×10^7	1.2	1.5×10^{-2}	4.7	3.6×10^{-2}	22	0.11
3×10^7	3×10^7	3.3	5.8×10^{-2}	26	0.15	240	0.51
1×10^8	1×10^7	∞	0.83	∞	2.6	∞	12
1×10^8	3×10^7	∞	5.0	∞	17	∞	260

TABLE IV: Median, 5% and 95% quantiles of the estimated measurement errors on m_2 for different mass configurations at redshift $z = 1$ without considering alternative theory parameters.

$m_1[M_\odot]$	$m_2[M_\odot]$	$\Delta m_2/m_2$ without corrections					
		5%-quantile		Median		95%-quantile	
		RWF	FWF	RWF	FWF	RWF	FWF
3×10^5	3×10^4	8.0×10^{-5}	5.9×10^{-5}	2.3×10^{-4}	1.7×10^{-4}	1.7×10^{-3}	1.7×10^{-3}
3×10^5	1×10^5	1.5×10^{-4}	1.2×10^{-4}	6.3×10^{-4}	3.7×10^{-4}	6.7×10^{-3}	6.7×10^{-3}
3×10^5	3×10^5	2.1×10^{-4}	1.3×10^{-4}	1.2×10^{-3}	2.9×10^{-4}	9.2×10^{-3}	9.2×10^{-3}
1×10^6	1×10^5	1.6×10^{-4}	1.1×10^{-4}	5.0×10^{-4}	3.0×10^{-4}	3.6×10^{-3}	3.6×10^{-3}
1×10^6	3×10^5	3.1×10^{-4}	2.2×10^{-4}	1.1×10^{-3}	6.9×10^{-4}	1.1×10^{-2}	1.1×10^{-2}
1×10^6	1×10^6	3.6×10^{-4}	2.7×10^{-4}	2.5×10^{-3}	6.9×10^{-4}	3.2×10^{-2}	3.2×10^{-2}
3×10^6	3×10^5	3.1×10^{-4}	1.7×10^{-4}	8.5×10^{-4}	4.7×10^{-4}	1.0×10^{-2}	1.0×10^{-2}
3×10^6	1×10^6	7.8×10^{-4}	4.2×10^{-4}	3.2×10^{-3}	9.7×10^{-4}	3.2×10^{-2}	3.2×10^{-2}
3×10^6	3×10^6	1.0×10^{-3}	3.7×10^{-4}	8.5×10^{-3}	8.2×10^{-4}	0.11	0.11
1×10^7	1×10^6	1.1×10^{-3}	4.0×10^{-4}	3.3×10^{-3}	1.0×10^{-3}	3.3×10^{-2}	3.3×10^{-2}
1×10^7	3×10^6	3.1×10^{-3}	7.3×10^{-4}	1.4×10^{-2}	1.5×10^{-3}	0.13	0.13
1×10^7	1×10^7	2.4×10^{-2}	2.1×10^{-3}	0.2	5.5×10^{-3}	1.6	1.6
3×10^7	3×10^6	3.5×10^{-2}	2.5×10^{-3}	0.13	5.0×10^{-3}	0.53	0.53
3×10^7	1×10^7	0.43	5.9×10^{-3}	1.5	1.3×10^{-2}	5.1	5.1
3×10^7	3×10^7	2.9	5.1×10^{-2}	19	0.13	130	130
1×10^8	1×10^7	∞	0.36	∞	1.0	∞	∞
1×10^8	3×10^7	∞	3.4	∞	9.9	∞	∞

TABLE V: Median, 5% and 95% quantiles of the estimated measurement errors on χ_1 for different mass configurations at redshift $z = 1$ with alternative theory parameters included.

$m_1[M_\odot]$	$m_2[M_\odot]$	$\Delta\chi_1$ with corrections					
		5%-quantile		Median		95%-quantile	
		RWF	FWF	RWF	FWF	RWF	FWF
3×10^5	3×10^4	3.3×10^{-4}	2.2×10^{-4}	9.7×10^{-4}	6.7×10^{-4}	4.3×10^{-3}	2.6×10^{-3}
3×10^5	1×10^5	8.3×10^{-4}	5.6×10^{-4}	3.1×10^{-3}	2.0×10^{-3}	1.6×10^{-2}	1.0×10^{-2}
3×10^5	3×10^5	2.1×10^{-3}	1.6×10^{-3}	1.3×10^{-2}	8.9×10^{-3}	0.24	0.14
1×10^6	1×10^5	6.6×10^{-4}	4.3×10^{-4}	1.9×10^{-3}	1.2×10^{-3}	7.9×10^{-3}	4.4×10^{-3}
1×10^6	3×10^5	1.6×10^{-3}	1.0×10^{-3}	4.9×10^{-3}	3.0×10^{-3}	2.3×10^{-2}	1.2×10^{-2}
1×10^6	1×10^6	3.5×10^{-3}	2.6×10^{-3}	3.4×10^{-2}	2.0×10^{-2}	0.61	0.21
3×10^6	3×10^5	1.3×10^{-3}	7.1×10^{-4}	3.5×10^{-3}	1.9×10^{-3}	1.7×10^{-2}	6.7×10^{-3}
3×10^6	1×10^6	3.1×10^{-3}	1.3×10^{-3}	1.4×10^{-2}	5.1×10^{-3}	6.9×10^{-2}	2.5×10^{-2}
3×10^6	3×10^6	1.5×10^{-2}	6.5×10^{-3}	0.17	5.2×10^{-2}	2.8	0.65
1×10^7	1×10^6	5.0×10^{-3}	1.4×10^{-3}	1.7×10^{-2}	4.4×10^{-3}	6.9×10^{-2}	1.5×10^{-2}
1×10^7	3×10^6	1.2×10^{-2}	2.3×10^{-3}	6.4×10^{-2}	9.5×10^{-3}	0.32	4.9×10^{-2}
1×10^7	1×10^7	0.68	8.6×10^{-2}	4.2	0.47	23	2.9
3×10^7	3×10^6	9.6×10^{-2}	6.1×10^{-3}	0.41	2.2×10^{-2}	2.0	6.5×10^{-2}
3×10^7	1×10^7	1.6	2.1×10^{-2}	4.6	0.11	17	0.44
3×10^7	3×10^7	14	2.9	79	11	780	61
1×10^8	1×10^7	∞	0.75	∞	2.6	∞	9.0
1×10^8	3×10^7	∞	8.9	∞	25	∞	240

TABLE VI: Median, 5% and 95% quantiles of the estimated measurement errors on χ_1 for different mass configurations at redshift $z = 1$ without considering alternative theory parameters.

$m_1[M_\odot]$	$m_2[M_\odot]$	$\Delta\chi_1$ without corrections					
		5%-quantile		Median		95%-quantile	
		RWF	FWF	RWF	FWF	RWF	FWF
3×10^5	3×10^4	1.8×10^{-4}	1.1×10^{-4}	4.2×10^{-4}	2.5×10^{-4}	1.6×10^{-3}	1.6×10^{-3}
3×10^5	1×10^5	4.6×10^{-4}	2.8×10^{-4}	1.4×10^{-3}	8.1×10^{-4}	9.3×10^{-3}	9.3×10^{-3}
3×10^5	3×10^5	1.0×10^{-3}	7.8×10^{-4}	6.0×10^{-3}	3.6×10^{-3}	8.8×10^{-2}	8.8×10^{-2}
1×10^6	1×10^5	3.6×10^{-4}	1.9×10^{-4}	8.7×10^{-4}	4.4×10^{-4}	2.9×10^{-3}	2.9×10^{-3}
1×10^6	3×10^5	8.6×10^{-4}	4.8×10^{-4}	2.2×10^{-3}	1.2×10^{-3}	1.2×10^{-2}	1.2×10^{-2}
1×10^6	1×10^6	1.6×10^{-3}	1.2×10^{-3}	1.2×10^{-2}	6.6×10^{-3}	0.19	0.19
3×10^6	3×10^5	4.8×10^{-4}	2.3×10^{-4}	1.2×10^{-3}	5.6×10^{-4}	5.8×10^{-3}	5.8×10^{-3}
3×10^6	1×10^6	1.3×10^{-3}	6.2×10^{-4}	4.2×10^{-3}	1.7×10^{-3}	3.2×10^{-2}	3.2×10^{-2}
3×10^6	3×10^6	4.4×10^{-3}	2.5×10^{-3}	4.0×10^{-2}	1.4×10^{-2}	0.92	0.92
1×10^7	1×10^6	1.3×10^{-3}	4.4×10^{-4}	3.5×10^{-3}	1.0×10^{-3}	1.5×10^{-2}	1.5×10^{-2}
1×10^7	3×10^6	3.5×10^{-3}	1.1×10^{-3}	1.5×10^{-2}	3.0×10^{-3}	0.1	0.1
1×10^7	1×10^7	0.12	2.1×10^{-2}	1.1	0.12	9.3	9.3
3×10^7	3×10^6	3.4×10^{-2}	2.7×10^{-3}	0.15	6.8×10^{-3}	0.63	0.63
3×10^7	1×10^7	0.46	9.4×10^{-3}	1.8	3.4×10^{-2}	7.5	7.5
3×10^7	3×10^7	12	1.3	63	5.1	520	520
1×10^8	1×10^7	∞	0.3	∞	1.3	∞	∞
1×10^8	3×10^7	∞	4.0	∞	14	∞	∞

TABLE VII: Median, 5% and 95% quantiles of the estimated measurement errors on χ_2 for different mass configurations at redshift $z = 1$ with alternative theory parameters included.

$m_1[M_\odot]$	$m_2[M_\odot]$	$\Delta\chi_2$ with corrections					
		5%-quantile		Median		95%-quantile	
		RWF	FWF	RWF	FWF	RWF	FWF
3×10^5	3×10^4	1.4×10^{-3}	8.9×10^{-4}	1.3×10^{-2}	9.0×10^{-3}	0.13	7.2×10^{-2}
3×10^5	1×10^5	2.0×10^{-3}	1.3×10^{-3}	9.7×10^{-3}	6.7×10^{-3}	8.9×10^{-2}	5.0×10^{-2}
3×10^5	3×10^5	2.0×10^{-3}	1.5×10^{-3}	1.4×10^{-2}	9.0×10^{-3}	0.25	0.13
1×10^6	1×10^5	3.3×10^{-3}	1.9×10^{-3}	2.7×10^{-2}	1.7×10^{-2}	0.32	0.15
1×10^6	3×10^5	3.4×10^{-3}	2.2×10^{-3}	1.8×10^{-2}	1.2×10^{-2}	0.13	5.7×10^{-2}
1×10^6	1×10^6	3.9×10^{-3}	2.7×10^{-3}	3.1×10^{-2}	1.9×10^{-2}	0.76	0.23
3×10^6	3×10^5	5.4×10^{-3}	2.7×10^{-3}	4.4×10^{-2}	2.4×10^{-2}	0.59	0.2
3×10^6	1×10^6	6.0×10^{-3}	2.6×10^{-3}	3.9×10^{-2}	1.9×10^{-2}	0.31	0.11
3×10^6	3×10^6	1.4×10^{-2}	6.7×10^{-3}	0.18	5.2×10^{-2}	2.7	0.66
1×10^7	1×10^6	1.9×10^{-2}	5.5×10^{-3}	0.17	5.1×10^{-2}	1.5	0.35
1×10^7	3×10^6	2.5×10^{-2}	4.8×10^{-3}	0.16	3.5×10^{-2}	1.4	0.26
1×10^7	1×10^7	0.72	9.6×10^{-2}	4.3	0.49	25	2.9
3×10^7	3×10^6	0.31	2.3×10^{-2}	4.0	0.24	33	1.3
3×10^7	1×10^7	2.6	4.3×10^{-2}	15	0.34	75	1.7
3×10^7	3×10^7	15	3.3	79	11	670	51
1×10^8	1×10^7	∞	3.0	∞	25	∞	140
1×10^8	3×10^7	∞	27	∞	120	∞	1.2×10^3

TABLE VIII: Median, 5% and 95% quantiles of the estimated measurement errors on χ_2 for different mass configurations at redshift $z = 1$ without considering alternative theory parameters.

$m_1[M_\odot]$	$m_2[M_\odot]$	$\Delta\chi_2$ without corrections					
		5%-quantile		Median		95%-quantile	
		RWF	FWF	RWF	FWF	RWF	FWF
3×10^5	3×10^4	7.6×10^{-4}	4.5×10^{-4}	2.7×10^{-3}	1.6×10^{-3}	1.5×10^{-2}	1.5×10^{-2}
3×10^5	1×10^5	8.2×10^{-4}	5.3×10^{-4}	3.3×10^{-3}	1.9×10^{-3}	1.9×10^{-2}	1.9×10^{-2}
3×10^5	3×10^5	1.0×10^{-3}	8.2×10^{-4}	6.3×10^{-3}	3.7×10^{-3}	7.9×10^{-2}	7.9×10^{-2}
1×10^6	1×10^5	1.6×10^{-3}	7.7×10^{-4}	5.6×10^{-3}	2.9×10^{-3}	3.3×10^{-2}	3.3×10^{-2}
1×10^6	3×10^5	1.4×10^{-3}	8.6×10^{-4}	5.0×10^{-3}	2.9×10^{-3}	2.9×10^{-2}	2.9×10^{-2}
1×10^6	1×10^6	1.6×10^{-3}	1.1×10^{-3}	1.2×10^{-2}	6.4×10^{-3}	0.23	0.23
3×10^6	3×10^5	2.3×10^{-3}	1.2×10^{-3}	7.6×10^{-3}	3.9×10^{-3}	5.8×10^{-2}	5.8×10^{-2}
3×10^6	1×10^6	2.2×10^{-3}	1.1×10^{-3}	7.9×10^{-3}	3.7×10^{-3}	6.4×10^{-2}	6.4×10^{-2}
3×10^6	3×10^6	4.0×10^{-3}	2.4×10^{-3}	4.1×10^{-2}	1.4×10^{-2}	0.88	0.88
1×10^7	1×10^6	6.2×10^{-3}	2.0×10^{-3}	3.1×10^{-2}	9.1×10^{-3}	0.19	0.19
1×10^7	3×10^6	7.8×10^{-3}	2.5×10^{-3}	3.4×10^{-2}	9.5×10^{-3}	0.17	0.17
1×10^7	1×10^7	0.13	2.1×10^{-2}	1.2	0.12	9.6	9.6
3×10^7	3×10^6	0.13	8.6×10^{-3}	1.3	6.5×10^{-2}	6.9	6.9
3×10^7	1×10^7	0.59	2.0×10^{-2}	4.5	0.1	24	24
3×10^7	3×10^7	14	1.2	66	5.1	450	450
1×10^8	1×10^7	∞	1.4	∞	13	∞	∞
1×10^8	3×10^7	∞	8.1	∞	48	∞	∞

TABLE IX: Median, 5% and 95% quantiles of the estimated measurement errors on $2a$ for different mass configurations at redshift $z = 1$ with alternative theory parameters included.

$m_1[M_\odot]$	$m_2[M_\odot]$	$2a[']$ with corrections					
		5%-quantile		Median		95%-quantile	
		RWF	FWF	RWF	FWF	RWF	FWF
3×10^5	3×10^4	7.5	4.5	21	13	83	67
3×10^5	1×10^5	5.3	3.3	24	15	99	81
3×10^5	3×10^5	6.9	4.3	29	21	110	100
1×10^6	1×10^5	12	8.2	37	22	130	96
1×10^6	3×10^5	11	7.2	36	23	140	100
1×10^6	1×10^6	11	6.7	47	34	180	140
3×10^6	3×10^5	16	8.0	40	21	160	100
3×10^6	1×10^6	15	7.3	51	27	220	150
3×10^6	3×10^6	15	7.6	74	40	420	260
1×10^7	1×10^6	27	8.9	87	28	440	130
1×10^7	3×10^6	26	8.8	130	41	700	190
1×10^7	1×10^7	58	18	459	130	4.4×10^3	930
3×10^7	3×10^6	160	23	640	77	7.5×10^3	350
3×10^7	1×10^7	459	43	5.0×10^3	190	8.1×10^4	1.2×10^3
3×10^7	3×10^7	1.6×10^4	670	3.8×10^5	3.9×10^3	7.9×10^6	2.3×10^4
1×10^8	1×10^7	∞	2.3×10^3	∞	8.4×10^3	∞	5.0×10^4
1×10^8	3×10^7	∞	1.7×10^4	∞	8.7×10^4	∞	6.6×10^5

TABLE X: Median, 5% and 95% quantiles of the estimated measurement errors on $2a$ for different mass configurations at redshift $z = 1$ without considering alternative theory parameters.

$m_1[M_\odot]$	$m_2[M_\odot]$	$2a[']$ without corrections					
		5%-quantile		Median		95%-quantile	
		RWF	FWF	RWF	FWF	RWF	FWF
3×10^5	3×10^4	7.2	4.4	20	13	77	77
3×10^5	1×10^5	5.0	3.1	21	14	91	91
3×10^5	3×10^5	6.0	3.7	26	18	100	100
1×10^6	1×10^5	8.5	7.6	35	20	120	120
1×10^6	3×10^5	8.5	6.2	33	21	120	120
1×10^6	1×10^6	8.3	5.6	38	26	150	150
3×10^6	3×10^5	9.6	6.8	35	19	140	140
3×10^6	1×10^6	11	6.3	41	23	190	190
3×10^6	3×10^6	11	5.7	51	28	280	280
1×10^7	1×10^6	18	7.6	64	24	300	300
1×10^7	3×10^6	20	7.8	87	32	420	420
1×10^7	1×10^7	34	13	220	83	1.8×10^3	1.8×10^3
3×10^7	3×10^6	100	20	380	64	3.0×10^3	3.0×10^3
3×10^7	1×10^7	180	27	1.3×10^3	120	1.5×10^4	1.5×10^4
3×10^7	3×10^7	4.7×10^3	400	1.3×10^5	2.2×10^3	2.2×10^6	2.2×10^6
1×10^8	1×10^7	∞	1.4×10^3	∞	4.5×10^3	∞	∞
1×10^8	3×10^7	∞	7.1×10^3	∞	3.3×10^4	∞	∞

TABLE XI: Median, 5% and 95% quantiles of the estimated measurement errors on $2b$ for different mass configurations at redshift $z = 1$ with alternative theory parameters included.

$m_1[M_\odot]$	$m_2[M_\odot]$	$2b[']$ with corrections					
		5%-quantile		Median		95%-quantile	
		RWF	FWF	RWF	FWF	RWF	FWF
3×10^5	3×10^4	0.98	0.57	4.7	2.7	13	7.3
3×10^5	1×10^5	0.9	0.52	4.1	2.4	17	9.3
3×10^5	3×10^5	1.5	0.89	5.8	3.4	22	15
1×10^6	1×10^5	2.3	1.0	11	5.0	28	13
1×10^6	3×10^5	1.8	1.1	9.0	4.8	30	17
1×10^6	1×10^6	2.0	1.1	9.7	5.8	39	27
3×10^6	3×10^5	2.4	1.2	11	5.4	31	14
3×10^6	1×10^6	2.1	1.0	10	4.9	34	16
3×10^6	3×10^6	2.2	1.1	12	5.7	56	30
1×10^7	1×10^6	3.4	1.1	17	5.6	66	16
1×10^7	3×10^6	3.9	1.4	19	6.1	87	25
1×10^7	1×10^7	14	4.3	64	18	310	93
3×10^7	3×10^6	29	3.8	110	15	919	56
3×10^7	1×10^7	88	10	600	34	6.1×10^3	140
3×10^7	3×10^7	1.2×10^3	93	2.9×10^4	530	6.3×10^5	3.0×10^3
1×10^8	1×10^7	∞	490	∞	1.8×10^3	∞	8.2×10^3
1×10^8	3×10^7	∞	3.2×10^3	∞	1.3×10^4	∞	9.2×10^4

TABLE XII: Median, 5% and 95% quantiles of the estimated measurement errors on $2b$ for different mass configurations at redshift $z = 1$ without considering alternative theory parameters.

$m_1[M_\odot]$	$m_2[M_\odot]$	$2b[']$ without corrections					
		5%-quantile		Median		95%-quantile	
		RWF	FWF	RWF	FWF	RWF	FWF
3×10^5	3×10^4	0.95	0.55	4.6	2.6	12	12
3×10^5	1×10^5	0.82	0.44	3.8	2.1	15	15
3×10^5	3×10^5	1.2	0.69	5.1	3.0	19	19
1×10^6	1×10^5	2.1	0.91	10	4.7	25	25
1×10^6	3×10^5	1.5	0.92	8.4	4.4	27	27
1×10^6	1×10^6	1.6	0.97	8.7	5.1	34	34
3×10^6	3×10^5	2.3	1.1	11	5.1	27	27
3×10^6	1×10^6	1.9	0.89	9.0	4.3	29	29
3×10^6	3×10^6	1.7	0.83	9.7	4.6	38	38
1×10^7	1×10^6	2.8	0.91	15	4.9	41	41
1×10^7	3×10^6	2.7	0.99	14	4.9	54	54
1×10^7	1×10^7	6.1	2.3	27	10	130	130
3×10^7	3×10^6	15	2.5	60	12	260	260
3×10^7	1×10^7	43	4.8	170	18	919	919
3×10^7	3×10^7	550	49	4.2×10^3	250	7.1×10^4	7.1×10^4
1×10^8	1×10^7	∞	270	∞	890	∞	∞
1×10^8	3×10^7	∞	1.4×10^3	∞	4.9×10^3	∞	∞

TABLE XIII: Median, 5% and 95% quantiles of the estimated measurement errors on d_L for different mass configurations at redshift $z = 1$ with alternative theory parameters included.

$m_1[M_\odot]$	$m_2[M_\odot]$	$\Delta d_L/d_L$ with corrections					
		5%-quantile		Median		95%-quantile	
		RWF	FWF	RWF	FWF	RWF	FWF
3×10^5	3×10^4	2.4×10^{-3}	1.5×10^{-3}	4.8×10^{-3}	3.0×10^{-3}	1.4×10^{-2}	8.8×10^{-3}
3×10^5	1×10^5	2.3×10^{-3}	1.5×10^{-3}	4.9×10^{-3}	3.3×10^{-3}	1.8×10^{-2}	1.2×10^{-2}
3×10^5	3×10^5	2.7×10^{-3}	2.0×10^{-3}	7.0×10^{-3}	5.1×10^{-3}	2.1×10^{-2}	1.7×10^{-2}
1×10^6	1×10^5	3.7×10^{-3}	2.5×10^{-3}	8.0×10^{-3}	5.0×10^{-3}	2.2×10^{-2}	1.4×10^{-2}
1×10^6	3×10^5	3.0×10^{-3}	2.3×10^{-3}	7.6×10^{-3}	5.1×10^{-3}	2.4×10^{-2}	1.6×10^{-2}
1×10^6	1×10^6	3.8×10^{-3}	2.7×10^{-3}	1.1×10^{-2}	7.6×10^{-3}	3.4×10^{-2}	2.6×10^{-2}
3×10^6	3×10^5	4.9×10^{-3}	3.3×10^{-3}	9.9×10^{-3}	6.3×10^{-3}	3.1×10^{-2}	1.6×10^{-2}
3×10^6	1×10^6	5.3×10^{-3}	3.2×10^{-3}	1.2×10^{-2}	7.5×10^{-3}	4.0×10^{-2}	2.4×10^{-2}
3×10^6	3×10^6	6.9×10^{-3}	4.1×10^{-3}	2.3×10^{-2}	1.3×10^{-2}	7.6×10^{-2}	4.1×10^{-2}
1×10^7	1×10^6	1.6×10^{-2}	6.4×10^{-3}	3.7×10^{-2}	1.4×10^{-2}	0.11	3.2×10^{-2}
1×10^7	3×10^6	2.8×10^{-2}	6.9×10^{-3}	7.1×10^{-2}	1.7×10^{-2}	0.23	5.2×10^{-2}
1×10^7	1×10^7	0.23	4.3×10^{-2}	0.71	9.4×10^{-2}	3.1	0.23
3×10^7	3×10^6	0.89	3.5×10^{-2}	4.4	8.0×10^{-2}	21	0.18
3×10^7	1×10^7	9.3	0.11	43	0.26	210	0.73
3×10^7	3×10^7	1.3×10^3	4.2	2.8×10^4	11	3.0×10^5	50
1×10^8	1×10^7	∞	16	∞	78	∞	560
1×10^8	3×10^7	∞	229	∞	1.0×10^3	∞	1.9×10^4

TABLE XIV: Median, 5% and 95% quantiles of the estimated measurement errors on d_L for different mass configurations at redshift $z = 1$ without considering alternative theory parameters.

$m_1[M_\odot]$	$m_2[M_\odot]$	$\Delta d_L/d_L$ without corrections					
		5%-quantile		Median		95%-quantile	
		RWF	FWF	RWF	FWF	RWF	FWF
3×10^5	3×10^4	1.1×10^{-3}	7.8×10^{-4}	2.5×10^{-3}	1.5×10^{-3}	9.4×10^{-3}	9.4×10^{-3}
3×10^5	1×10^5	9.2×10^{-4}	6.1×10^{-4}	2.8×10^{-3}	1.7×10^{-3}	1.4×10^{-2}	1.4×10^{-2}
3×10^5	3×10^5	1.2×10^{-3}	7.7×10^{-4}	4.3×10^{-3}	2.8×10^{-3}	1.8×10^{-2}	1.8×10^{-2}
1×10^6	1×10^5	1.9×10^{-3}	9.8×10^{-4}	5.0×10^{-3}	2.5×10^{-3}	1.8×10^{-2}	1.8×10^{-2}
1×10^6	3×10^5	1.7×10^{-3}	1.1×10^{-3}	4.9×10^{-3}	2.8×10^{-3}	2.0×10^{-2}	2.0×10^{-2}
1×10^6	1×10^6	1.8×10^{-3}	1.1×10^{-3}	6.8×10^{-3}	4.4×10^{-3}	2.7×10^{-2}	2.7×10^{-2}
3×10^6	3×10^5	2.0×10^{-3}	1.2×10^{-3}	5.1×10^{-3}	2.7×10^{-3}	2.2×10^{-2}	2.2×10^{-2}
3×10^6	1×10^6	2.0×10^{-3}	1.2×10^{-3}	5.9×10^{-3}	3.2×10^{-3}	2.9×10^{-2}	2.9×10^{-2}
3×10^6	3×10^6	2.1×10^{-3}	1.3×10^{-3}	8.7×10^{-3}	4.9×10^{-3}	4.6×10^{-2}	4.6×10^{-2}
1×10^7	1×10^6	3.1×10^{-3}	1.3×10^{-3}	8.4×10^{-3}	3.4×10^{-3}	4.0×10^{-2}	4.0×10^{-2}
1×10^7	3×10^6	4.0×10^{-3}	2.0×10^{-3}	1.2×10^{-2}	4.8×10^{-3}	7.2×10^{-2}	7.2×10^{-2}
1×10^7	1×10^7	1.4×10^{-2}	6.9×10^{-3}	6.2×10^{-2}	2.2×10^{-2}	0.31	0.31
3×10^7	3×10^6	3.0×10^{-2}	4.9×10^{-3}	8.0×10^{-2}	1.0×10^{-2}	0.49	0.49
3×10^7	1×10^7	0.23	1.6×10^{-2}	0.76	3.5×10^{-2}	3.2	3.2
3×10^7	3×10^7	3.3	0.21	21	0.5	380	380
1×10^8	1×10^7	∞	0.44	∞	1.1	∞	∞
1×10^8	3×10^7	∞	3.1	∞	9.4	∞	∞

TABLE XV: Median, 5% and 95% quantiles of the estimated measurement errors on Ψ_{-1} for different mass configurations at redshift $z = 1$

$m_1[M_\odot]$	$m_2[M_\odot]$	$\Delta\Psi_{-1}$					
		5%-quantile		Median		95%-quantile	
		RWF	FWF	RWF	FWF	RWF	FWF
3×10^5	3×10^4	3.0×10^{-6}	1.8×10^{-6}	7.3×10^{-6}	5.4×10^{-6}	7.0×10^{-5}	4.9×10^{-5}
3×10^5	1×10^5	2.8×10^{-6}	1.8×10^{-6}	7.3×10^{-6}	6.0×10^{-6}	5.2×10^{-5}	4.6×10^{-5}
3×10^5	3×10^5	5.3×10^{-6}	3.2×10^{-6}	1.5×10^{-5}	1.1×10^{-5}	1.2×10^{-4}	8.2×10^{-5}
1×10^6	1×10^5	1.4×10^{-5}	5.9×10^{-6}	3.3×10^{-5}	2.2×10^{-5}	2.9×10^{-4}	2.2×10^{-4}
1×10^6	3×10^5	1.4×10^{-5}	7.8×10^{-6}	3.6×10^{-5}	2.6×10^{-5}	2.3×10^{-4}	1.8×10^{-4}
1×10^6	1×10^6	5.3×10^{-5}	2.2×10^{-5}	1.4×10^{-4}	8.8×10^{-5}	6.3×10^{-4}	4.0×10^{-4}
3×10^6	3×10^5	9.8×10^{-5}	3.1×10^{-5}	2.1×10^{-4}	1.1×10^{-4}	1.2×10^{-3}	6.1×10^{-4}
3×10^6	1×10^6	1.9×10^{-4}	3.1×10^{-5}	4.2×10^{-4}	1.6×10^{-4}	1.1×10^{-3}	6.1×10^{-4}
3×10^6	3×10^6	8.2×10^{-4}	1.4×10^{-4}	2.6×10^{-3}	7.0×10^{-4}	8.0×10^{-3}	2.1×10^{-3}
1×10^7	1×10^6	2.9×10^{-3}	3.8×10^{-4}	6.4×10^{-3}	9.3×10^{-4}	1.6×10^{-2}	2.8×10^{-3}
1×10^7	3×10^6	7.3×10^{-3}	3.4×10^{-4}	1.9×10^{-2}	1.9×10^{-3}	5.5×10^{-2}	4.8×10^{-3}
1×10^7	1×10^7	6.1×10^{-2}	1.0×10^{-2}	0.18	2.4×10^{-2}	0.77	6.3×10^{-2}
3×10^7	3×10^6	0.25	8.3×10^{-3}	1.3	1.7×10^{-2}	7.6	4.5×10^{-2}
3×10^7	1×10^7	2.9	4.3×10^{-2}	15	0.11	74	0.29
3×10^7	3×10^7	459	1.5	9.1×10^3	4.0	9.1×10^4	18
1×10^8	1×10^7	∞	4.6	∞	24	∞	210
1×10^8	3×10^7	∞	75	∞	400	∞	7.5×10^3

TABLE XVI: Median, 5% and 95% quantiles of the estimated measurement errors on Ψ_0 for different mass configurations at redshift $z = 1$

$m_1[M_\odot]$	$m_2[M_\odot]$	$\Delta\Psi_0$					
		5%-quantile		Median		95%-quantile	
		RWF	FWF	RWF	FWF	RWF	FWF
3×10^5	3×10^4	1.4×10^{-3}	7.0×10^{-4}	3.1×10^{-3}	2.1×10^{-3}	1.7×10^{-2}	1.3×10^{-2}
3×10^5	1×10^5	1.3×10^{-3}	8.1×10^{-4}	3.2×10^{-3}	2.4×10^{-3}	1.4×10^{-2}	1.3×10^{-2}
3×10^5	3×10^5	2.2×10^{-3}	1.2×10^{-3}	5.9×10^{-3}	4.1×10^{-3}	3.1×10^{-2}	2.3×10^{-2}
1×10^6	1×10^5	4.7×10^{-3}	1.7×10^{-3}	1.0×10^{-2}	6.2×10^{-3}	6.3×10^{-2}	4.7×10^{-2}
1×10^6	3×10^5	4.6×10^{-3}	2.4×10^{-3}	1.2×10^{-2}	7.9×10^{-3}	5.3×10^{-2}	3.9×10^{-2}
1×10^6	1×10^6	1.5×10^{-2}	5.4×10^{-3}	3.8×10^{-2}	2.3×10^{-2}	0.13	9.1×10^{-2}
3×10^6	3×10^5	2.1×10^{-2}	5.7×10^{-3}	4.6×10^{-2}	2.5×10^{-2}	0.21	0.11
3×10^6	1×10^6	3.7×10^{-2}	4.7×10^{-3}	8.5×10^{-2}	3.5×10^{-2}	0.22	0.11
3×10^6	3×10^6	0.13	1.1×10^{-2}	0.38	0.11	1.1	0.34
1×10^7	1×10^6	0.31	4.6×10^{-2}	0.76	0.14	2.1	0.38
1×10^7	3×10^6	0.73	2.7×10^{-2}	2.0	0.25	5.8	0.66
1×10^7	1×10^7	4.8	0.96	14	2.3	60	6.2
3×10^7	3×10^6	8.4	0.73	71	1.8	530	4.4
3×10^7	1×10^7	96	3.5	800	9.1	4.4×10^3	26
3×10^7	3×10^7	1.1×10^4	110	2.7×10^5	290	3.3×10^6	1.2×10^3
1×10^8	1×10^7	∞	160	∞	1.2×10^3	∞	1.4×10^4
1×10^8	3×10^7	∞	2.6×10^3	∞	2.2×10^4	∞	4.6×10^5

TABLE XVII: Median, 5% and 95% quantiles of the estimated measurement errors on $\Psi_{1/2}$ for different mass configurations at redshift $z = 1$

$m_1[M_\odot]$	$m_2[M_\odot]$	$\Delta\Psi_{1/2}$					
		5%-quantile		Median		95%-quantile	
		RWF	FWF	RWF	FWF	RWF	FWF
3×10^5	3×10^4	1.5×10^{-2}	5.7×10^{-3}	3.6×10^{-2}	2.0×10^{-2}	0.13	9.6×10^{-2}
3×10^5	1×10^5	1.4×10^{-2}	7.0×10^{-3}	3.3×10^{-2}	2.3×10^{-2}	0.13	0.11
3×10^5	3×10^5	1.8×10^{-2}	1.0×10^{-2}	5.0×10^{-2}	3.6×10^{-2}	0.24	0.18
1×10^6	1×10^5	3.9×10^{-2}	1.5×10^{-2}	8.7×10^{-2}	4.8×10^{-2}	0.4	0.3
1×10^6	3×10^5	3.5×10^{-2}	2.0×10^{-2}	9.1×10^{-2}	6.2×10^{-2}	0.35	0.27
1×10^6	1×10^6	0.1	3.4×10^{-2}	0.27	0.16	0.9	0.59
3×10^6	3×10^5	0.13	4.0×10^{-2}	0.29	0.16	1.2	0.66
3×10^6	1×10^6	0.22	3.6×10^{-2}	0.52	0.21	1.3	0.67
3×10^6	3×10^6	0.65	6.3×10^{-2}	2.0	0.6	6.0	1.9
1×10^7	1×10^6	1.3	0.23	3.6	0.78	10	2.1
1×10^7	3×10^6	3.2	0.15	9.0	1.3	28	3.5
1×10^7	1×10^7	19	4.0	56	10	250	29
3×10^7	3×10^6	21	2.9	240	7.7	2.0×10^3	22
3×10^7	1×10^7	200	14	2.6×10^3	37	1.4×10^4	110
3×10^7	3×10^7	1.9×10^4	409	5.7×10^5	1.1×10^3	6.8×10^6	5.0×10^3
1×10^8	1×10^7	∞	330	∞	3.5×10^3	∞	5.1×10^4
1×10^8	3×10^7	∞	5.6×10^3	∞	7.1×10^4	∞	1.5×10^6

TABLE XVIII: Median, 5% and 95% quantiles of the estimated measurement errors on Ψ_1 for different mass configurations at redshift $z = 1$

$m_1[M_\odot]$	$m_2[M_\odot]$	$\Delta\Psi_1$					
		5%-quantile		Median		95%-quantile	
		RWF	FWF	RWF	FWF	RWF	FWF
3×10^5	3×10^4	0.14	3.6×10^{-2}	0.32	0.16	0.91	0.61
3×10^5	1×10^5	0.15	4.5×10^{-2}	0.33	0.21	1.0	0.74
3×10^5	3×10^5	0.19	6.0×10^{-2}	0.48	0.29	1.6	1.4
1×10^6	1×10^5	0.3	7.5×10^{-2}	0.65	0.34	2.0	1.3
1×10^6	3×10^5	0.27	0.11	0.67	0.4	1.8	1.2
1×10^6	1×10^6	0.49	0.13	1.3	0.68	4.4	2.9
3×10^6	3×10^5	0.61	0.16	1.4	0.74	4.0	2.4
3×10^6	1×10^6	0.79	0.13	1.9	0.84	5.0	2.7
3×10^6	3×10^6	1.3	0.2	4.0	1.4	15	5.9
1×10^7	1×10^6	3.1	0.5	8.8	2.4	25	6.0
1×10^7	3×10^6	5.2	0.34	14	2.4	45	8.1
1×10^7	1×10^7	28	5.5	76	13	320	36
3×10^7	3×10^6	62	6.1	560	15	3.6×10^3	35
3×10^7	1×10^7	400	17	3.7×10^3	46	2.0×10^4	120
3×10^7	3×10^7	4.2×10^4	440	7.1×10^5	1.1×10^3	1.2×10^7	5.1×10^3
1×10^8	1×10^7	∞	1.0×10^3	∞	8.0×10^3	∞	8.3×10^4
1×10^8	3×10^7	∞	8.5×10^3	∞	9.0×10^4	∞	1.8×10^6

TABLE XIX: Median, 5% and 95% quantiles of the estimated measurement errors on $\Psi_{3/2}$ for different mass configurations at redshift $z = 1$

$m_1[M_\odot]$	$m_2[M_\odot]$	$\Delta\Psi_{3/2}$					
		5%-quantile		Median		95%-quantile	
		RWF	FWF	RWF	FWF	RWF	FWF
3×10^5	3×10^4	1.1	0.13	2.5	1.4	8.2	6.3
3×10^5	1×10^5	1.3	0.16	3.0	1.9	8.7	7.3
3×10^5	3×10^5	2.0	0.22	5.1	2.9	16	14
1×10^6	1×10^5	2.8	0.24	6.1	3.4	23	15
1×10^6	3×10^5	3.0	0.63	7.5	4.5	21	14
1×10^6	1×10^6	6.8	0.71	17	8.9	47	32
3×10^6	3×10^5	7.5	0.71	18	9.7	53	33
3×10^6	1×10^6	11	0.42	27	11	66	33
3×10^6	3×10^6	20	1.1	54	18	160	63
1×10^7	1×10^6	35	3.7	110	32	330	77
1×10^7	3×10^6	58	1.5	180	34	600	110
1×10^7	1×10^7	250	61	770	150	3.6×10^3	459
3×10^7	3×10^6	450	66	3.7×10^3	190	3.1×10^4	459
3×10^7	1×10^7	3.4×10^3	160	2.8×10^4	500	1.7×10^5	1.5×10^3
3×10^7	3×10^7	3.5×10^5	3.6×10^3	3.2×10^6	1.0×10^4	4.1×10^7	4.7×10^4
1×10^8	1×10^7	∞	8.7×10^3	∞	5.4×10^4	∞	6.5×10^5
1×10^8	3×10^7	∞	7.2×10^4	∞	6.8×10^5	∞	1.4×10^7

TABLE XX: Median, 5% and 95% quantiles of the estimated measurement errors on Ψ_2 for different mass configurations at redshift $z = 1$

$m_1[M_\odot]$	$m_2[M_\odot]$	$\Delta\Psi_2$					
		5%-quantile		Median		95%-quantile	
		RWF	FWF	RWF	FWF	RWF	FWF
3×10^5	3×10^4	4.0	0.35	8.9	5.3	30	23
3×10^5	1×10^5	5.1	0.6	12	7.6	34	28
3×10^5	3×10^5	8.2	0.83	21	12	63	52
1×10^6	1×10^5	10	0.76	23	13	86	55
1×10^6	3×10^5	12	2.1	30	18	85	54
1×10^6	1×10^6	26	2.7	65	33	180	120
3×10^6	3×10^5	26	1.9	63	35	180	110
3×10^6	1×10^6	38	1.3	97	40	250	120
3×10^6	3×10^6	60	3.0	170	58	520	210
1×10^7	1×10^6	84	9.3	320	110	1.0×10^3	240
1×10^7	3×10^6	130	3.9	450	100	1.7×10^3	340
1×10^7	1×10^7	509	130	1.6×10^3	350	8.8×10^3	1.1×10^3
3×10^7	3×10^6	890	190	7.5×10^3	490	6.3×10^4	1.2×10^3
3×10^7	1×10^7	9.5×10^3	380	4.6×10^4	1.0×10^3	2.9×10^5	3.1×10^3
3×10^7	3×10^7	5.4×10^5	5.7×10^3	5.5×10^6	1.7×10^4	8.3×10^7	8.7×10^4
1×10^8	1×10^7	∞	2.8×10^4	∞	1.3×10^5	∞	1.3×10^6
1×10^8	3×10^7	∞	2.0×10^5	∞	1.2×10^6	∞	2.4×10^7

[1] C. M. Will, Living Reviews in Relativity **9** (2006), arXiv:gr-qc/0510072.
[2] C. Brans and R. H. Dicke, Phys. Rev. **124**, 925 (1961).
[3] J. Bekenstein and M. Milgrom, Astrophys. J. **286**, 7 (1984).
[4] J. D. Bekenstein, Phys. Rev. D **70**, 083509 (2004).
[5] V. Faraoni, ArXiv e-prints (2008), arXiv:0810.2602v1.
[6] C. M. Will, Phys. Rev. D **57**, 2061 (1998).
[7] A. Stavridis and C. M. Will, Phys. Rev. D **80**, 044002 (2009).
[8] N. Yunes and F. Pretorius, Phys. Rev. D **80**, 122003 (2009).
[9] P. Amaro-Seoane, S. Aoudia, S. Babak, P. Binétruy, E. Berti, A. Bohé, C. Caprini, M. Colpi, N. J. Cornish, K. Danzmann, et al., Classical and Quantum Gravity **29**, 124016 (2012).
[10] L. S. Finn, Phys. Rev. D **46**, 5236 (1992).
[11] E. Poisson and C. M. Will, Phys. Rev. D **52**, 848 (1995).
[12] C. M. Will, Phys. Rev. D **50**, 6058 (1994).
[13] P. D. Scharre and C. M. Will, Phys. Rev. D **65**, 042002 (2002).
[14] E. Berti, A. Buonanno, and C. M. Will, Phys. Rev. D **71**, 084025 (2005).
[15] K. Yagi and T. Tanaka, Phys. Rev. D **81**, 064008 (2010).
[16] K. G. Arun and C. M. Will, Classical and Quantum Gravity **26**, 155002 (2009).
[17] D. Keppel and P. Ajith, Phys. Rev. D **82**, 122001 (2010).
[18] E. Berti, J. Gair, and A. Sesana, Phys. Rev. D **84**, 101501 (2011).
[19] K. G. Arun, B. R. Iyer, M. S. S. Qusailah, and B. S. Sathyaprakash, Classical and Quantum Gravity **23**, L37 (2006).
[20] N. Cornish, L. Sampson, N. Yunes, and F. Pretorius, Phys. Rev. D **84**, 062003 (2011).
[21] L. Blanchet, Living Reviews in Relativity **9** (2006), arXiv:gr-qc/9903107.
[22] L. Blanchet, A. Buonanno, and G. Faye, Phys. Rev. D **74**, 104034 (2006).
[23] T. A. Apostolatos, C. Cutler, G. J. Sussman, and K. S. Thorne, Phys. Rev. D **49**, 6274 (1994).
[24] K. G. Arun, A. Buonanno, G. Faye, and E. Ochsner, Phys. Rev. D **79**, 104023 (2009).
[25] E. Komatsu, J. Dunkley, M. R. Nolta, C. L. Bennett, B. Gold, G. Hinshaw, N. Jarosik, D. Larson, M. Limon, L. Page, et al., Astrophysical Journal Supplement Series **180**, 330 (2009).
[26] C. M. Will, *Theory and Experiment in Gravitational Physics* (Cambridge University Press, Cambridge, England, 1993).
[27] K. S. Thorne, Reviews of Modern Physics **52**, 299 (1980).
[28] L. Blanchet, G. Faye, B. R. Iyer, and B. Joguet, Phys. Rev. D **65**, 061501 (2002).
[29] A. Klein, P. Jetzer, and M. Sereno, Phys. Rev. D **80**, 064027 (2009).
[30] N. Yunes, K. G. Arun, E. Berti, and C. M. Will, Phys. Rev. D **80**, 084001 (2009).
[31] S. Droz, D. J. Knapp, E. Poisson, and B. J. Owen, Phys. Rev. D **59**, 124016 (1999).
[32] N. Yunes and S. A. Hughes, Phys. Rev. D **82**, 082002 (2010).
[33] C. Cutler and É. E. Flanagan, Phys. Rev. D **49**, 2658 (1994).
[34] M. Vallisneri, Phys. Rev. D **77**, 042001 (2008).
[35] T. B. Littenberg and N. J. Cornish, Phys. Rev. D **80**, 063007 (2009).
[36] T. G. F. Li, W. Del Pozzo, S. Vitale, C. Van Den Broeck, M. Agathos, J. Veitch, K. Grover, T. Sidery, R. Sturani, and A. Vecchio, Phys. Rev. D **85**, 082003 (2012).
[37] K. G. Arun, S. Babak, E. Berti, N. Cornish, C. Cutler, J. Gair, S. A. Hughes, B. R. Iyer, R. N. Lang, I. Mandel, et al., Classical and Quantum Gravity **26**, 094027 (2009).
[38] R. N. Lang and S. A. Hughes, Phys. Rev. D **74**, 122001 (2006).
[39] C. Cutler, Phys. Rev. D **57** (1998).
[40] A. Vecchio and E. D. Wickham, Phys. Rev. D **70**, 082002 (2004).
[41] N. Seto, Phys. Rev. D **66**, 122001 (2002).
[42] L. J. Rubbo, N. J. Cornish, and O. Poujade, Phys. Rev. D **69**, 082003 (2004).
[43] R. N. Lang, S. A. Hughes, and N. J. Cornish, Phys. Rev. D **84**, 022002 (2011).
[44] S. Alexander and N. Yunes, Phys. Rep. **480**, 1 (2009).
[45] K. Chatziioannou, N. Yunes, and N. Cornish, ArXiv e-prints (2012), arXiv:1204.2585.
[46] A. Buonanno, Y. Chen, and M. Vallisneri, Phys. Rev. D **67**, 104025 (2003).
[47] L. E. Kidder, C. M. Will, and A. G. Wiseman, Phys. Rev. D **47**, 4183 (1993).
[48] L. E. Kidder, Phys. Rev. D **52**, 821 (1995).
[49] A. Buonanno, Y. Chen, and M. Vallisneri, Phys. Rev. D **67**, 024016 (2003).
[50] N. J. Cornish and J. S. Key, Phys. Rev. D **82**, 044028 (2010).
[51] L. Blanchet, B. R. Iyer, and B. Joguet, Phys. Rev. D **65**, 064005 (2002).
[52] L. Blanchet, T. Damour, and G. Esposito-Farèse, Phys. Rev. D **69**, 124007 (2004).
[53] L. Blanchet, T. Damour, G. Esposito-Farèse, and B. R. Iyer, Phys. Rev. D **71**, 124004 (2005).